CHARACTERIZATION OF INCLINED OSCILLATING JETS AND CROSSFLOW INTERACTION FOR USE IN ACTIVE FLOW CONTROL

BY

VANESSA G. AWATE

THESIS

Submitted in partial fulfillment of the requirements
for the degree of Master of Science in Aerospace Engineering
in the Graduate College of the
University of Illinois at Urbana-Champaign, 2020

Urbana, Illinois

Adviser:

Assistant Professor Phillip J. Ansell

Abstract

Phase-locked stereoscopic PIV measurements were conducted to understand the interaction of inclined fluidic oscillator jets with a crossflow across a range of different blowing ratios. The fluidic oscillators used in the current study featured rounded internal feedback channels and produced spatially oscillating jets at predictable frequencies. When integrated into aerodynamic bodies, fluidic oscillators have the potential to re-energize boundary layers and delay the onset of flow separation at high angles of attack. Understanding the effects of blowing ratios and inclination angles on mixing characteristics and turbulent interactions in the flow can shed light on the effectiveness of such fluidic oscillators for active flow control purposes. Fluidic oscillators with an aspect ratio of 2 and inclination angles of 30°, 60° and 90° were designed and tested at different mass flow rates through the jet for a given freestream condition. The variation in the subsequent interactions produced with varying jet velocity and inclination angle, relative to the crossflow, were considered. For the investigated blowing ratios, the development and convection of high momentum regions and vortices were observed across the flow field. For higher blowing ratios, the downstream propagation of these structures was accompanied by larger spanwise and wall-normal jet penetration into the boundary layer due to higher turbulence interactions. Preliminary results for inclination angles of 60° and 90° revealed that the inclination angle affected the formation of vortices in the flow field and suggested that a combination of blowing ratio 5 and inclination angle of 60° would be an appropriate starting point for active flow control with fluidic oscillators.

Acknowledgements

I would first like to thank my advisor, Dr. Phillip Ansell, for his guidance and support over the last two years. His patience and tutelage were instumental to the completion of this work and I have truly enjoyed learning and working along side him.

I am also grateful for the financial support I have received from different entities within the University of Illinois at Urbana-Champaign and for the opportunity to pursue my graduate studies and expand my knowledge and appreciation of aerodynamics.

I would like to thank all of my labmates for their kindness and their willingness to share their holistic knowledge. I am particularly grateful to Rohit Gupta and Georgi Hristov for all of their help and the stimulating discussions about fluid mechanics, mathematics and laser diagnostics.

Finally, I would like to thank God, my family and friends for being my strength and my joy. *Maman*, thank you for your inspiring faith and your words of wisdom. *Papa*, thank you for your exemplary work ethic and for always pushing me to think more critically about the world and physics. To my sisters, thank you for being my personal cheerleaders. I truly am because we are.

Table of Contents

List of Figures

List of Tables

Nomenclature

List of Symbols

α	Jet inclination angle
AR	Aspect ratio at the outlet throat
A_{ss}	Cross-section area of the wind tunnel settling section
A_{ts}	Cross-section area of the wind tunnel test section
BR	Blowing Ratio
β	Jet Skew angle
dt	Time interval between consecutive laser pulses
$\Delta\boldsymbol{\tau}$	Time delay for at given phase angle
∂	Partial derivative
f	focal length (mm)
f	Oscillation frequency
l_{o}	Fluidic oscillator outlet length
l_{t}	Fluidic oscillator inlet throat length
l_{w}	Fluidic oscillator wedge length
$\dot{m}$	Mass flow rate through an individual oscillator
μ	Dynamic Viscosity
N	Number of samples
P	Pressure
ρ_{amb}	Ambient density
Q	Q-criterion
q_{∞}	Freestream Dynamic pressure
σ_V	Scatter in the mean flow velocity
R	Specific ideal gas constant
R_{xy}, R_{zy}	Reynolds shear stresses
R_{xx}	Reynolds normal stress
S_X	Standard deviation of N observations
t	Fluidic oscillator thickness

t^*	Student t-statistic
T_{amb}	Ambient temperature
U_{ss}	Settling section velocity
U_{ts}, U_∞	Test section velocity, freestream velocity
U_{jet}	Oscillator jet velocity
u	Velocity
U	Local velocity or Uncertainty
$\dot{v}$	Volume flow rate through an individual oscillator
ϕ	Phase angle of jet during oscillation cycle
ω_x	Streamwise Vorticity
x	Independent variable
$\overline{X_n}$	Mean of N observations

Abbreviations

CAD	Computer Aided Design
CFD	Computational Fluid Dynamics
FFT	Fast Fourier Transform
FOV	Field of View
FSM	Frame Straddling Mode
FTLE	Finite-Time Lyapunov Exponent
NI-DAQ	National Instruments Data Acquisition board
RANS	Reynolds-Averaged Navier Stokes
RPM	Revolutions Per Minutes
sCMOS	Complementary Metal Oxide Semiconductor
SLPM	Standard Liters Per Minute
sPIV	Stereoscopic Particle Image Velocimetry
TKE	Turbulent Kinetic Energy
TTL	Transistor-Transistor Logic

Chapter 1 Introduction

Fluidic oscillators, also known as flip-flop jet nozzles, have gained increased attention in recent decades within the flow control community. Their mechanical simplicity and the self-sustained oscillating nature of their jets make them attractive actuation devices. These fluid logic devices were developed by the US Army Harry Diamond Laboratories in the 1960s and are primarily used with liquids as their working fluid. Current usage of those devices for liquid distribution includes shower heads, sprinkles, and windshield cleaner systems. In such devices, the supplied flow initially enters a mixing chamber through an inlet nozzle and forms a jet that attaches to one of the inner walls (Fig. 1.1). Then, part of the jet is directed to the outlet at a certain angle known as the deflection angle. A small portion of the fluid stream tube is directed into an adjacent feedback channel and re-enters the mixing chamber, causing the formation of a circulation bubble between the wall and the attached jet. As the fluid continues its loop through the feedback channels, the circulation bubble grows and eventually detaches the jet from the wall. The jet switches side and attaches to the opposite inner wall of the mixing chamber, and the process continues, creating a self-sustained sweeping jet oscillation. The internal geometry of the fluidic oscillator dictates the rate at which fluid circulates through the feedback channels, and thus governs the jet oscillation process. Early studies of these jets in a quiescent environment revealed that oscillating jets have a significantly higher entrainment rate than steady jets[2, 3, 4]. This sparked further investigations with the intent of using these fluidic actuators for separation control[5,6], heat transfer and combustion mixing enhancement[7,8], and noise control[9], among other applications. To effectively target the naturally occurring instabilities in such flows and to increase the effectiveness of the unsteady actuation, a better understanding of the interactions between a crossflow and different fluidic oscillator jets is required.

1.1 Literature Review

Previous experimental works that investigated oscillator jets in crossflows focused on one inclination angle and different blowing ratios (BRs). The inclination angle was defined as the angle between the oscillation plane and the crossflow. Ostermann et al.[10] presented time-averaged and time-resolved PIV data of a fluidic oscillator ejecting into a turbulent boundary layer at a 90° inclination angle (normal to the surface) with a blowing ratio BR = 3. Internal oscillator pressure tap data was acquired simultaneously with the PIV snapshots and used as a reference signal to develop a phase averaging method. This approach resulted in time-resolved data that showed the evolution of the jet in the streamwise direction. These authors found that the jet penetrates the crossflow more at its sides, where the jet deflection angle with respect to the oscillator centerline-tangent is highest. The bi-stable effect and longer dwelling times experienced at such locations due to the attachment of the jet to the exit wall, are the driving mechanisms behind such downstream propagation at the sides. The jet wall-normal trajectory was also shallower than a steady jet due the faster velocity decay of oscillating jets while the lateral spreading was considerably larger due to the sweeping motion of the jets. The time-averaged results showed the presence of dominant streamwise vortex structures. Those vortices were found to have a sense of rotation opposite to those produced by a steady jet interaction with a crossflow, which is thought to keep the vortices closer to the wall further downstream. Ostermann et al.[11,12] extended the previous study to include different blowing ratios, and thus frequencies. In addition to Eulerian methods, Lagrangian techniques were used to track the trajectory of particles across instantaneous PIV images and to produce instantaneous streak volumes and FTLE flow field visualizations for each phase angle. As the blowing ratio increased, both the spanwise and streamwise penetrations of the jet into the crossflow became more pronounced and a larger area was affected downstream of the jet exit. The wall-normal penetration, normalized by a product of blowing ratio and oscillator hydraulic diameter, was identical across the blowing ratios, suggesting a strong dependency of penetration height on the blowing ratio parameter. The vortex pair observed in their previous study was pushed away from the wall and the oscillator centerline for higher blowing ratios. A decrease in maximum vorticity accompanied by a growth in vortex size was also observed. Therefore, the separation between vortices became shorter and the vortices remained around the same location throughout one oscillation cycle. For cases with BR $\geq$ 5, a second pair of vortices emerged between the jet and the wall with their sense of rotation being

opposite to the first pair. The formation of this second vortex pair was attributed to the larger timescale differences between the jet and the crossflow as the blowing ratios were increased. In addition to the dominant streamwise vortices, which prevailed far downstream, spanwise and wall normal vortices were identified in the near field of the jet exit. These two studies showed the influence of blowing ratio on the generation and propagation of vortices and their induced velocities into a boundary layer.

A CFD study by Aram et al.[13] used a delayed detached-eddy simulation model to look at interactions between a sweeping jet and an attached turbulent crossflow. The results of this study were validated against the experimental results from Ostermann et al.[12]. Similar features were observed in terms of formation of larger alternating vortex pairs as the blowing ratio was increased from BR = 1 to BR = 3. The authors also noted an increase in penetration heights and lateral spreading as the blowing ratio was changed.

Other experiments considered the influence of skew angles and blowing ratios on the interaction between an oscillating jet and a crossflow[14]. The skew angles were defined as the angles between the jet's sweeping direction and the local crossflow, such that a skew angle of 90° also corresponded to an inclination angle of 90°. This study focused on skew angles, β, between 0° and 90° and showed the qualitative flow field characteristics as well as jet trajectories and the dynamics of the vortex formation process. For all the cases, small upstream effects were observed upstream of the oscillator exit due to the jet's alignment with respect to the crossflow. The wall-normal and spanwise penetrations varied significantly across skew angles due to changes in jet alignment with the crossflow. As skew angles became smaller, the component of the jet momentum in the spanwise direction decreased, leading to smaller spanwise area being affected. An opposite trend emerged for the wall-normal penetration heights as the jet switched to align with the crossflow at a given smaller skew angle. Shallower skew angles also introduced an asymmetry in the observed streamwise vortices across the flow field during a half oscillation cycle. Streamwise vortices became more persistent and propagated in the far field at phase angles for which the jet opposed the crossflow (i.e., turned into the flow) and disappeared when the jet partially aligned with the crossflow (i.e., turned away from the crossflow). For $\beta = 0°$, the vortex dynamics were different and no alternating streamwise vortices were identified. The vortices formed for that case were similar to that of an inclined steady jet, simultaneously occurring on both sides of the oscillator centerline. The authors found that $\beta = 90°$ was a more effective vortex

generator with farther lasting and stronger streamwise vortices. For all skew angles, the position and vorticity strength of the streamwise vortices were dependent on the angle between the jet and the wall as it swept through an oscillation, thus highlighting the importance of investigating inclination angle effects on vortex formation and propagation.

Another numerical study by Hossain et al.[15] investigated the flow interactions of an oscillating jet in a crossflow for different inclination angles and blowing ratios. FLUENT was used to perform unsteady RANS simulations on a curved fluidic oscillator jet in crossflow to obtain time-averaged and time-resolved flow fields. These results were validated qualitatively for and inclination angle $\alpha = 90°$ and BR = 3 through a comparison with experimental results from Ostermann et al[10,11,12]. In addition to the alternating vortex pairs found in Ostermann et al, smaller structures such as horseshoe vortices and ring-like vortices were found. Hossain et al. suggested that such structures might have been lost in the experimental results through spatial smoothing during the phase averaging process. The jet lateral spreading and penetration height were observed to increase with blowing ratio, and the streamlines bent away from the wall due to the larger and weaker streamwise vortices observed. These authors concluded that the crossflow interaction had no effect on the jet oscillation frequency, which was observed to be directly dependent on the internal structure of the oscillator. Improvements in mixing between the jet and crossflow were also observed with increasing blowing ratios. In addition to confirming Ostermann's observations for $\alpha = 90°$, the authors found that the coherent structures in the streamwise direction persisted for longer distances as the inclination angle decreased. For $\alpha = 30°$ and $\alpha = 60°$, the addition of streamwise velocity to the flow field due to the associated oscillator jet inclination was observed to allow these structures to remain for a longer time. However, the previously observed ring-like vortex structures were lost for the shallowest inclination angle of $\alpha = 30°$. The bending of streamlines towards the wall also occurred further downstream for shallower inclination angles. Across all inclination angles, the highest spanwise deflection of streamlines were observed for a phase angle of $\phi = 90°$, at which the jet left the exit with minimum deflection.

1.2 Research Motivation and Objectives

Previous parametric studies were performed to determine the effectiveness of different flow control techniques. Some of the considered active flow control devices included steady blowing jets, steady vortex generating jets and sweeping jet actuators. The results showed that

sweeping jet actuators were more effective than steady blowing and steady vortex generating jets thanks to their dual momentum addition and vortex generating nature[4,16]. Subsequent studies, which focused on the types of sweeping jet actuators and their frequency behavior, revealed that those with a rounded internal geometry have power spectra with well-defined frequency peaks compared to those with rectangular internal geometries[17]. For this reason, further studies on oscillating jets for active flow control purposes have focused on fluidic oscillators with a rounded internal geometry to provide more predictable frequencies for unsteady actuation. The current investigation aims to bridge the experimental gap on the interaction of such oscillating jets with a crossflow while providing additional insight for related computational studies on such flow configurations. The aforementioned studies suggested that actuators with large spreading area placed close to the separation region were more effective at controlling the flow than alternative configurations. An emphasis was also placed on streamwise vortices, outlining their prevalence and suggesting that they are of high interests for spatially oscillating jets. This work addresses the influence of inclination angles on the flow field, which previous studies have not investigated. In addition to that, the effects of blowing ratio combinations for a 30° inclined oscillating jet into a crossflow on the evolution of the streamwise vortices and the surrounding flow domain are characterized. The primary objectives of the current investigation can be summarized as follows:

- Characterize the three-dimensional flow field produced by an inclined fluidic oscillator jet in crossflow and quantify the jet spreading and wall-normal penetration.
- Identify streamwise vortices created by the oscillating jet in crossflow interaction across different phase angles and their effect on mixing.
- Obtain turbulence statistics and identify driving mechanisms behind more effective mixing.

1.3 Chapter 1 Figures

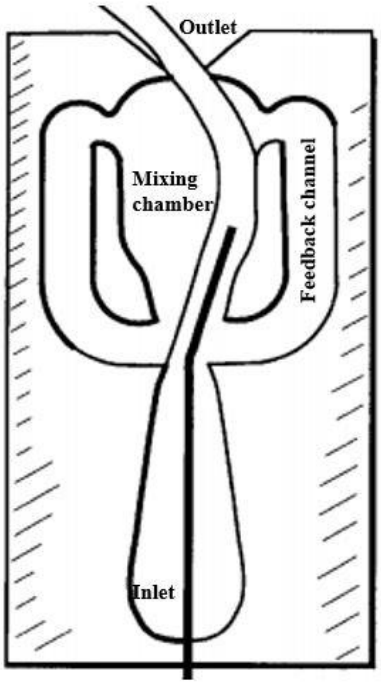

Fig. 1.1 Rounded fluidic oscillator with two feedback channels [1].

Chapter 2 Experimental Methods

This chapter describes the experimental methods, equipment and facilities used to conduct this study. It contains a detailed description of the experimental setup, data acquisition system and data reduction techniques.

2.1 Testing Environment

2.1.1 Wind tunnel

The experiments were conducted in a subsonic, open-return type wind tunnel, illustrated in Fig. 2.1. The wind tunnel had a streamwise length of 2.4 m and a rectangular test section with dimensions of 85.3 cm by 122 cm. To consider the boundary layer growth along the tunnel walls and its effect on the velocity across the test section, the tunnel was designed with a linearly expanding cross-sectional area in the streamwise direction. A contraction ratio of 7.5:1 between the settling region and the beginning of the test section was used to achieve a constant effective cross-sectional area across the test section. Additional features of the tunnel include a 10-cm thick honeycomb panel and four anti-turbulence screens located at the inlet of the tunnel, whose primary function was to straighten the incoming flow and to maintain the turbulence level below 0.1% during the operation of the wind tunnel. For the current study, the tunnel floor was equipped with an acrylic window that allow the laser sheet to access the flow field of interest within the test section.

A regulated 125-horsepower AC motor, powered by an ABB ACS 800 Low Voltage AC Drive, was used to drive the wind tunnel fan, located at the end of the diffuser section. The motor could produce angular velocities up to about 1200 RPM, thus enabling a maximum empty test section speed of approximately 265 km/h (73 m/s). In the present experiment, the motor speed was controlled using an iterative LabView routine designed to achieve a prescribed test section freestream velocity, which was kept within 0.5 % of the desired value during testing.

The test-section velocity was calculated using the static pressure difference between the inlet settling section and the test-section inlet ($P_{ss} - P_{ts}$). This pressure differential was measured using a Setra 239 15" WC pressure transducer. The recorded static pressures were obtained using a pair of static pressure rings, consisting of four different pressure taps located on each of the tunnel walls, at both the settling and test sections. Using the obtained pressure differential and assuming a steady, inviscid and incompressible flow across the tunnel, an expression for the test section speed (2.3) was derived from a combination of Bernoulli's equation (2.2) and the continuity equation (2.1) applied between the settling section and the test section inlet.

$$A_{ss}U_{ss} = A_{ts}U_{ts} \tag{2.1}$$

$$\frac{1}{2}\rho_{amb}U_{ss}^2 + P_{ss} = \frac{1}{2}\rho_{amb}U_{ts}^2 + P_{ts} \tag{2.2}$$

$$U_{ts} = \sqrt{\frac{2(P_{ss}-P_{ts})}{\rho_{amb}\left(1-\left(\frac{A_{ts}}{A_{ss}}\right)^2\right)}} \tag{2.3}$$

Where $\frac{A_{ts}}{A_{ss}}$ is the ratio of the test section to the settling section area, ρ_{amb} is the ambient air density, calculated using the ideal gas law (2.4)

$$\rho_{amb} = \frac{P_{amb}}{RT_{amb}} \tag{2.4}$$

where R is the specific ideal gas constant for air. The ambient pressure, P_{amb}, and temperature T_{amb} are measured using a Setra 270 absolute pressure transducer and a National Instrument Type-J thermocouple respectively.

2.2 Fluidic Oscillator Model and Flow Control System

The current study was performed using fluidic oscillators that featured rounded internal geometries and could produce oscillation frequencies between 40 Hz and 200 Hz, depending on the supplied mass flow rate of the pressure system. To maintain the similar mass flow rate across the oscillators, each fluidic oscillator was designed with an outlet throat aspect ratio of 2. The aspect ratio is defined as the ratio of the oscillator outlet length to the thickness of the oscillator centerpiece (2.5). In addition to that, each oscillator was designed to produce a specific inclination angle between their centerline-tangent and the cross flow. Inclination angles of 30°, 60° and 90°

were considered for this study. The oscillators were manufactured from aluminum in sets of three layers. A back and front plate were used as sealing faces to secure the oscillator geometry plate and attach it to the tunnel ceiling at the given inclination angle. Rubber gaskets, that would compress once the layers were tightened together, were placed on the sealing faces to minimize side leakage. Fig. 2.2 shows a CAD drawing of the fluidic oscillator assembly made up of the three aluminum plates.

$$AR = \frac{l_o}{t} \tag{2.5}$$

The oscillator was driven from a dedicated pressurized air source, supplied by an Ingersoll-Rand compressor and a low-pressure, high-volume (1034 kPa, 132 m^3) air storage system. When operating the fluidic oscillator, the compressed air from the tank farm was initially stepped down to 120 psi using a dedicated manual pressure regulator. The supply pressure was further reduced and controlled using an SMC ITV3050-31N4CL4 electronic pressure regulator, which takes in input voltages between 0 and 5V. The pressure regulator converts the voltage to input pressure percentages and can go up to 130 psi. Then, the flow conditions through the air supply to the fluidic oscillator were measured and recorded using an Omega model FMA-1613A mass flow meter (Fig. 2.3). The flow meter can measure flow rates up to 1250 SLPM and provided temperature, pressure, volume flow and mass flow measurements.

In addition to the inclination angles, the other driving parameter for the current experiment was the blowing ratio. The blowing ratio, $BR = U_{jet}/U_{\infty}$, is defined as the ratio of the oscillator jet velocity to that of the freestream. Three blowing ratios (BR = 3, 5 and 7) were considered but the jet velocity was kept under 102 m/s to satisfy an incompressible flow assumption. In order to achieve a desired blowing ratio, the necessary mass flow through the oscillator system was first calculated according to Eq. 2.6.

$$\dot{m} = U_{\infty} BR \rho_{amb} l_o t \tag{2.6}$$

where ρ_{amb} is the ambient air density in kg/m^3.

A programed closed loop system was used to control the mass flow through the oscillators. The pressure regulator was connected to a computer through a NI-DAQ 6009 board and powered by a DC power supply, while the mass flow meter was connected through a serial port to the computer. For a given blowing ratio, the desired mass flow rate was input and starting value was

assigned the pressure regulator. The current mass flow reading from the flow meter was then sent to the computer and compared against the target mass flow. While the desired value was not reached, within a prescribed tolerance, the computer sent a feedback signal and generated a new voltage setting that was transmitted through the NI-DAQ board to the pressure regulator. In order to reach the final mass flow, a convergence threshold was set within 0.5% of target mass flow rate. The mass flow rate was checked during each phase angle run and was reset as needed. Fig. 2.4 shows a flow chart detailing the routine for controlling the oscillator pressure. Section 2.3.4 provides details on the testing matrix and the parameters considered during the experiment.

2.3 Flow Diagnostics Method

Phase-locked stereoscopic Particle Image Velocimetry (sPIV) was used to study the 3D flow field produced by the interaction of the fluidic oscillator jet and the freestream without intruding on the flow or changing its characteristics. sPIV is an optical measurement technique in which the flow is seeded with small tracer particles that faithfully track the flow and whose velocity is measured to determine the velocity of the flow field. Those particles are illuminated with a high-intensity coherent source of light, most commonly a laser which emits two consecutive beam pulses, separated by a few microseconds. Then, consecutive image pairs of the illuminated the field of view (FOV) are recorded by two cameras at different instants of time, capturing the high-intensity light scattering produced by the seed particles. A cross correlation technique is then used between the image pairs to determine the most statistically likely displacement of particle clusters, allowing for the motion of the particles across the two image frames to be calculated. The instantaneous velocity fields are then calculated from the know time delay between the two image frames and the measured particle displacements. For phase-locked sPIV, the process is repeated with a trigger that is synchronized with a distinct characteristics phase in the studied flow field.

In this study, the flow was seeded with using a combination of a mineral oil-based haze generator, which produced particles with mean particle diameter of 1 to 2 μm and a ViCount compact 1300 smoke generator with particle diameter of 0.2 to 0.3 μm. The hazer particles were continuously introduced upstream of the open return tunnel. This made it possible to always maintain the particle density in the FOV at a reasonable level. The smoke particles were introduced immediately above the oscillator pneumatic supply part. Such a configuration allowed the particles to undergo the same motion as the flow throughout the oscillator, from the mixing chamber to the

far field away from the oscillator outlet. The phase-locked sPIV data were acquired at nine equidistant streamwise planes across the span of the oscillator outlet to obtain the three-dimensional velocity field (Fig. 2.5). The main components of the sPIV system described in this study consisted of a Nd:YAG dual pulse laser, two LaVision Imager sCMOS cameras, a microphone and a LaVision programmable time unit (PTU-X) used to synchronize the former devices and acquire phase-locked sPIV data through LaVision Davis 8.0 software package. An overview of the experimental setup is seen in Fig. 2.6.

2.3.1 Camera System

Two LaVision Imager scientific Complementary Metal Oxide Semiconductor (sCMOS) cameras were used to acquire digital images of the tracer particles in the flow. The cameras had a resolution of 2560×2160 pixels and recorded images onto two frames, with exposure times of 10μs and 19.981ms, respectively. The cameras were operated in Frame Straddling mode (FSM) which implied that the first laser pulse was fired towards the end first camera frame and the second laser pulse was fired at the beginning of the second frame (Fig. 2.7). The FSM allowed the choice of the pulse time delay, dt, to be decoupled from the camera frame rate, resulting in statistically independent PIV images. The cameras were fitted with two Nikon AF-Nikkor lenses (f =105 mm) oriented at angles less than 30° with respect to the center of the FOV to correct for the limitation in optical aperture caused by the relatively large focal length of the lenses. In addition to adjusting the lens plane, the lenses were both set to a f-number of 11 in order minimize risk of saturating the pixel arrays on the cameras. To increase the depth of field, Scheimpflug adapters were used to adjust the camera tilt angles and bring the camera image planes to the same focus as the laser plane according to the Scheimpflug condition (Fig. 2.8). The cameras were focused on the FOV, which was slightly skewed downstream of the oscillator outlet to visualize the convection of the flow structures along the tunnel ceiling. LaVision's self-calibration feature and a 3D type 106-10 calibration plate were used prior to data acquisition to correct for any registration disparities between the images acquired by camera 1 and 2.

2.3.2 Laser and Optics setup

The EverGreen laser is a dual-pumped 532nm Nd: YAG laser system that features precisely overlapped beams designed to minimize PIV correlation noise. It has a maximum energy of 200 mJ per pulse and a maximum repetition rate of 15 Hz. The vertical polarization of the laser along

with the high laser power made it possible to maintain an appropriate level of light intensity for the entire laser sheet, which spanned the region right upstream of the leading edge of the oscillator outlet (25.4 mm) and extended a total width of 190.5 mm. For the current experiment, the laser was operated with a time interval of dt = 60μs between laser pulses for the blowing ratios of 3 and 5 cases, with a time interval of dt = 50μs for BR = 7. This corresponded to a particle displacement of approximately 7 pixels in the freestream between images. In order to illuminate the FOV, a laser sheet was formed through a series of beamforming optics that were mounted on the wind tunnel balance. After leaving the laser head, the beam was passed through an aperture to remove the low-intensity fringes and provide a laser beam with a more uniform-intensity distribution. Then, a plano concave cylindrical lens of focal length f = -12.7 mm was used to expand the laser beam along the horizontal direction. Following was a plano convex cylindrical lens with f = 1000 mm, which was used to converge the beam into a sheet with enough thickness as to resolve the out-of-plane particle displacements between laser pulses. Finally, a dielectric mirror was used to re-orient the beam and create a sheet parallel to the freestream.

2.3.3 Trigger system

The trigger system consisted of a microphone, a signal conditioning unit, a pulse generator, and a LaVision programmable time unit (PTU-X). In order to provide a trigger to phase lock the sPIV acquisition, an analog signal was obtained from a microphone placed immediately downstream of the exit of the oscillator. This reference signal was then amplified using a signal conditioning unit and sent to an oscilloscope, a pulse generator and a computer. The BNC model 565 pulse generator was used to produce a Transistor-Transistor Logic (TTL) signal and was gated to exclusively pulse when the microphone output voltage exceeded a value corresponding to the oscillator jet overlapping with the microphone location. The pulse widths and gating voltages were chosen to ensure the rising portion of the microphone signal opened a new TTL signal that spanned an entire microphone signal cycle, and hence triggered the acquisition of one image pair for each TTL signal interval. The generated TTL signal varied with the jet oscillation frequency and thus with blowing ratio. The TTL signal was then sent to both the oscilloscope and to the trigger input of the PTU-X unit. The oscilloscope was primarily used to visualize signals and to aid in selecting the gating voltage to generate the TTL signal (Fig. 2.9). The microphone signal transferred to the computer directly from the signal conditioning unit was sampled for 10s at a frequency of 3000

Hz, which corresponded to a Nyquist frequency of 1500 Hz which was well above the jet oscillation frequencies for the investigated blowing ratios. The sampled signal was then sent to a LabView code, which generated power spectral density plots of the signal to extract the dominant frequency of the jet. For a given blowing ratio, the frequency value was validated using the FFT function of the oscilloscope and a predictive frequency model, which related the volume flow rate through the oscillator to the oscillation frequency and geometry design parameters (Eq. 2.7). This frequency was then used to establish delay times from the trigger signal and target a specific phase angle across an oscillation cycle (Eq. 2.8).

$$f = \frac{(\dot{v}AR)^{0.9624}}{e^{3.5439} l_o^{1.5151} l_t^{0.9980} l_w^{0.4019}} \tag{2.7}$$

$$\Delta\tau = \frac{\boldsymbol{\phi}}{360f} \tag{2.8}$$

where $\dot{v}$ is the volume flow rate, l_o, l_t, l_w are the oscillator outlet length, inlet/throat length and wedge length, respectively, f is the oscillation frequency of the jet, ϕ is the phase angle and $\boldsymbol{\Delta\tau}$ is the corresponding time delay.

The PTU-X unit was used apply the delay times to the incoming external TTL trigger signal and to synchronize the cameras and laser. A total of eight phase angles were captured across an entire oscillation cycle.

2.3.4 Data acquisition and experimental matrix

For a given oscillator inclination angle, three blowing ratios were investigated at a fixed freestream velocity, U_∞ = 12.5m/s. Each blowing ratio was set by varying the jet exit velocity, which resulted in a change in the reference oscillation frequency. Using the prescribed time delays, data were acquired for eight phase angles across the 30° inclined oscillating jet for each of those blowing ratios (Table 2.1). For the inclination angles of 60° and 90°, data were acquired for five phase angles across the oscillator outlet for BR = 3, 5 and 7 (Table 2.2).

To acquire data at different spanwise positions across the oscillator outlet, the cameras and beamforming optics were mounted on separate rails that were connected to a Zaber T-LSR150A and a Zaber T-LSR450B vertical traverse systems, respectively. The use of the Zaber systems allowed the cameras and optics to be moved simultaneously across the oscillator outlet while maintaining the camera focus on the illuminated particles across the moving laser sheet. A

LabView code, which took the desired survey plane as an input, was used to precisely move the Zabers by the same distance. That traversing distance was calculated from the width of the oscillator outlet and the respective micro step sizes of the Zabers. During each run, the tunnel velocity was first set. Then, the flow field was seeded, and the desired mass flow rate was entered into the tunnel computer. Once the target flow rate was reached, the tunnel freestream conditions, mass flow conditions, jet velocity, jet frequency and corresponding time delay for the desired phase angle were recorded. Then, DaVis PIV image acquisition software was used to record images. DaVis was operated using a double frame event and the external random trigger mode which allowed the incoming TTL signal to the PTU-X to be used as trigger. The obtained time delay, $\Delta\boldsymbol{\tau}$, was entered into the DaVis recording window as a reference time T1A, corresponding to the beginning of exposure for the first frame. The reference time T1B for the second frame was obtained by adding the desired laser pulse delay, dt, to the first reference time T1A. These reference times were transmitted to the cameras and laser as an offset from the trigger signal through the PTU-X unit. For each phase angle-blowing ratio-inclination angle combination, 700 instantaneous image pairs were acquired at each survey plane across the span of the oscillator.

After the image data were acquired, LaVision DaVis 8.4 processing software was used to determine the three-component velocity vector fields that corresponded to each instantaneous set of image pairs. The stereo cross-correlation technique used to obtain such fields featured a multipass reduction method. A squared interrogation window with an initial size of 128×128 pixels was used at the beginning of the correlation process with a 50% overlap and two initial passes. The final window size was decreased to a circular interrogation window within 32×32 pixels and provided a 75% overlap with 4 passes to find the correlation peak. High accuracy mode based on a B-spline-6 reconstruction was implemented for the final passes. A universal outlier detection median filter was then applied and 5×5 pixels regions with less than 5 vectors were removed. Finally, optimal smoothing and filling were used to obtain uniform instantaneous vector fields. A MATLAB code was used to further reduce the data and obtain phase-averaged flow fields.

2.4 Chapter 2 Figures

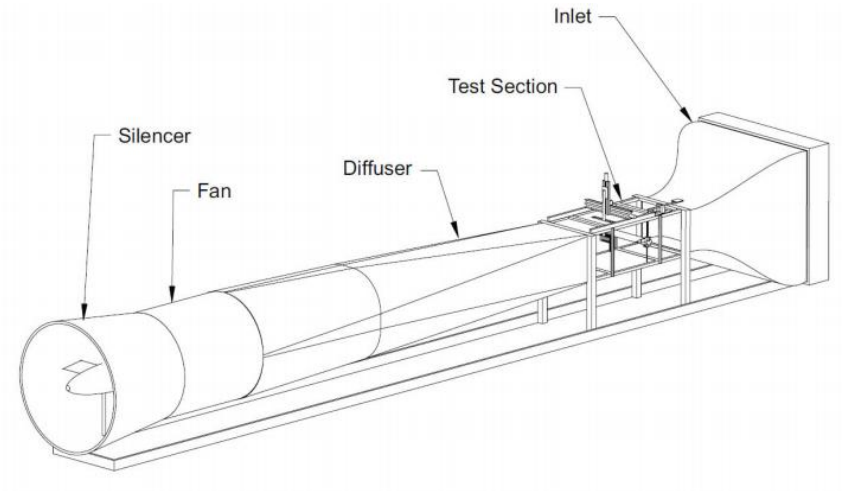

Fig. 2.1 Schematic of University of Illinois Subsonic 2.8-ft × 4-ft wind tunnel

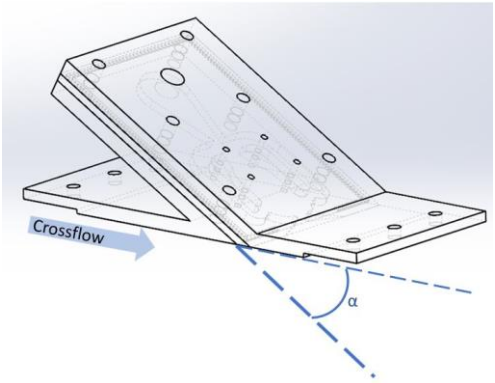

Fig. 2.2 CAD model of fluidic oscillator at a 30° inclination angle

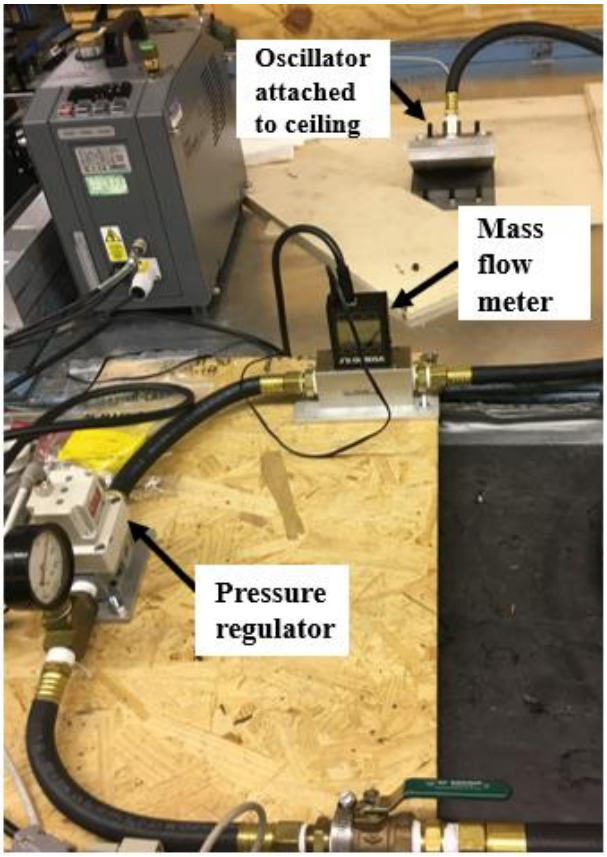

Fig. 2.3 Pressure system, consisting of a mass flow meter, pressure regulator, and oscillator configured to eject at a 30° angle into the wind tunnel ceiling

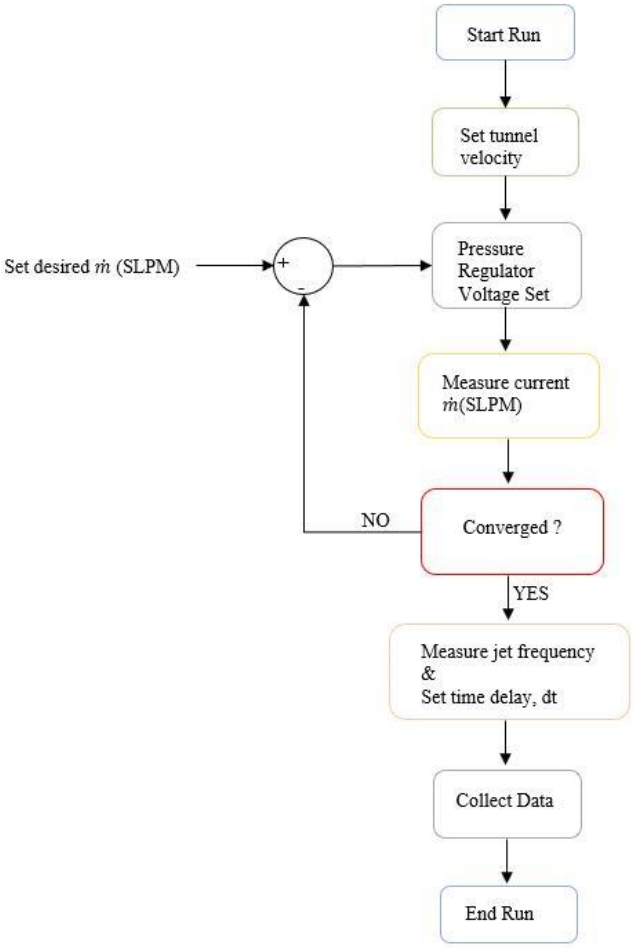

Fig. 2.4 Flow chart detailing the feedback control of the fluidic oscillators

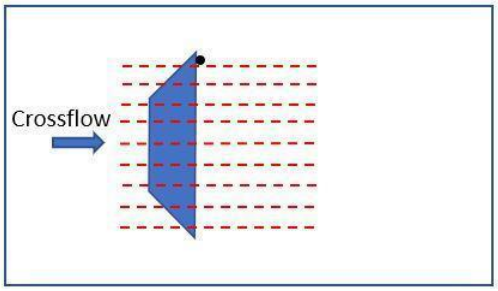

Fig. 2.5 sPIV acquisition planes across oscillator outlet with microphone location

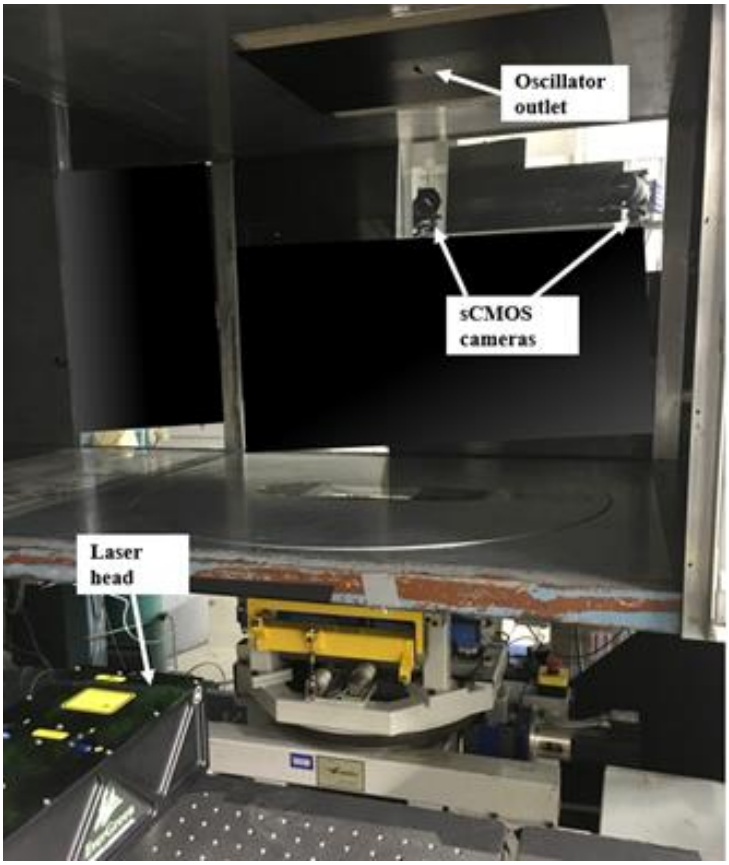

Fig. 2.6 sPIV configuration for oscillator in crossflow

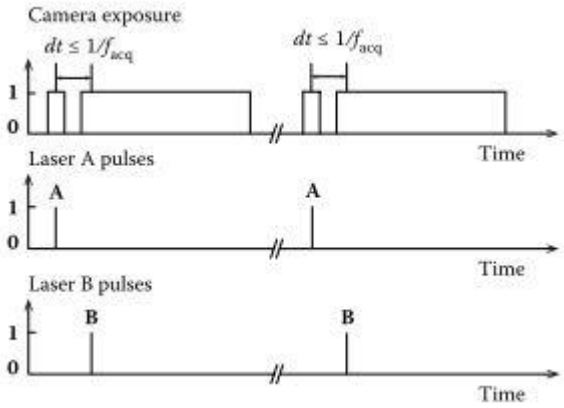

Fig. 2.7 Laser and camera timing sequences for FSM PIV with sCMOS cameras

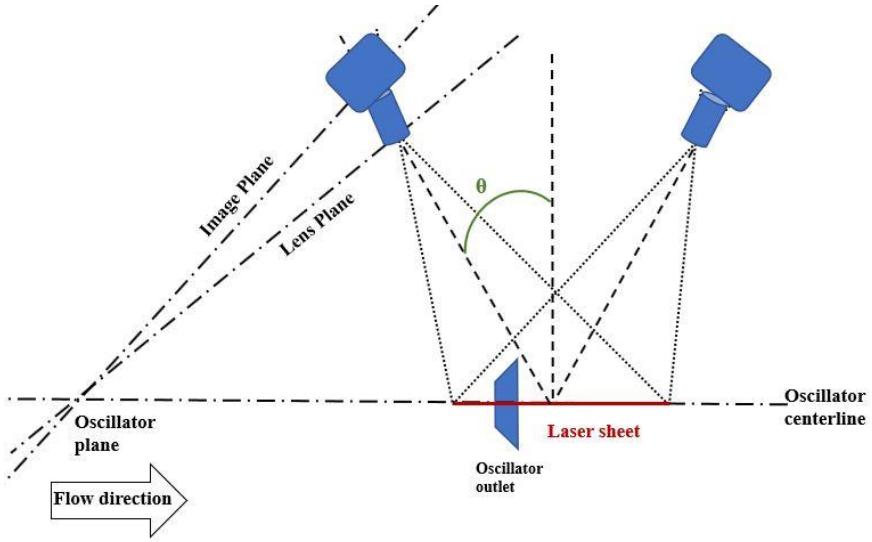

Fig. 2.8 Scheimpflug configuration for oscillator in crossflow sPIV setup

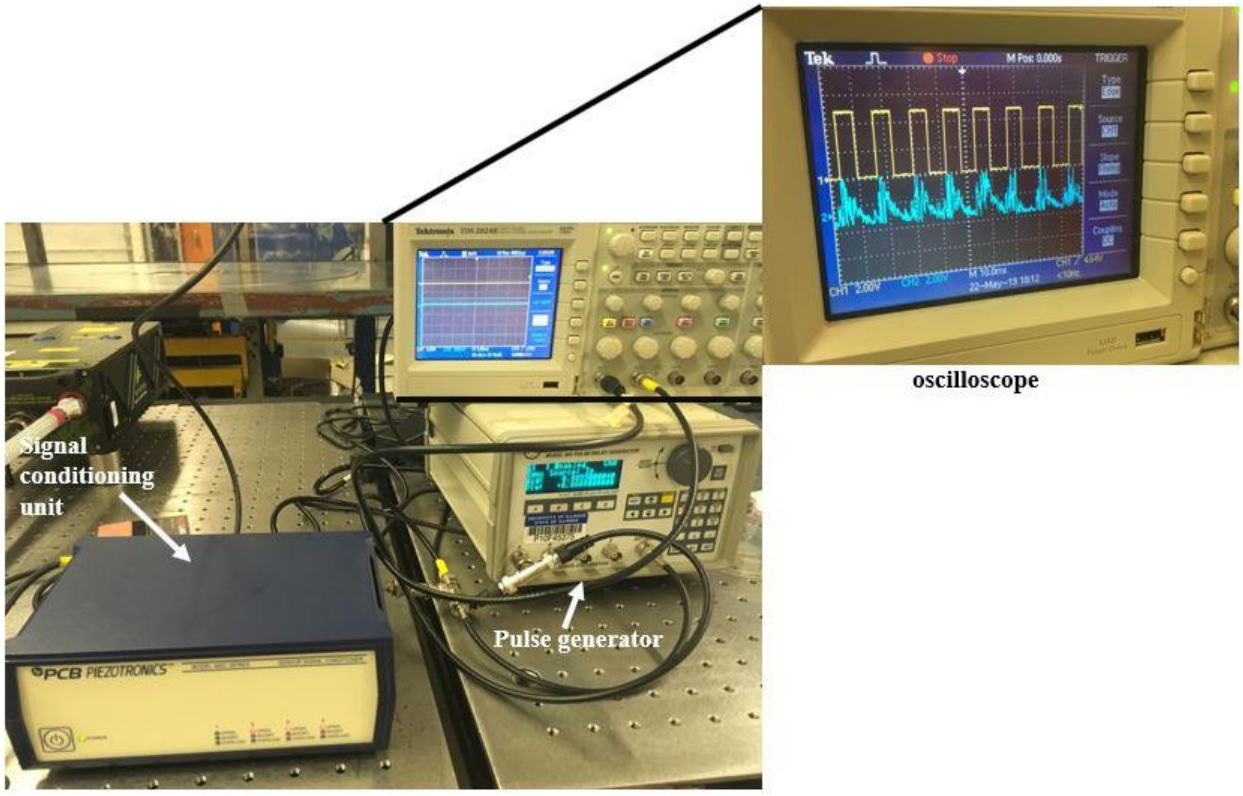

Fig. 2.9 Trigger system for sPIV phase locking process

2.5 Chapter 2 Tables

Table 2.1 Test matrix for fluidic oscillator inclined at $\alpha = 30°$.

Blowing ratios	Run 1	Run 2	Run 3	Run 4	Run 5	Run 6	Run 7	Run 8
BR = 3	ϕ = 19.8°	ϕ = 64.8°	ϕ = 109.8°	ϕ = 154.8°	ϕ = 199.8°	ϕ = 244.8°	ϕ = 289.8°	ϕ = 334.8°
BR = 5	ϕ = 23.4°	ϕ = 68.4°	ϕ = 113.4°	ϕ = 158.4°	ϕ = 203.4°	ϕ = 248.4°	ϕ = 293.4°	ϕ = 338.4°
BR = 7	ϕ = 28.8°	ϕ = 73.8°	ϕ = 118.8°	ϕ = 163.8°	ϕ = 208.8°	ϕ = 253.8°	ϕ = 298.8°	ϕ = 343.8°

Table 2.2 Test matrix for fluidic oscillator inclined at $\alpha = 60°$ and $\alpha = 90°$.

Blowing ratios	Run 1	Run 2	Run 3	Run 4	Run 5
BR = 3	ϕ = 19.8°	ϕ = 64.8°	ϕ = 109.8°	ϕ = 154.8°	ϕ = 199.8°
BR = 5	ϕ = 23.4°	ϕ = 68.4°	ϕ = 113.4°	ϕ = 158.4°	ϕ = 203.4°
BR = 7	ϕ = 28.8°	ϕ = 73.8°	ϕ = 118.8°	ϕ = 163.8°	ϕ = 208.8°

Chapter 3 Results and Discussion

3.1 Average Flow Fields

3.1.1 Statistical Convergence

For each of the investigated cases, 1400 image-pairs were recorded during the experiment, but due to computational time limits, sets of 700 image-pairs were post-processed. To verify the independence of such image pairs, a case study was performed for one run, consisting of BR=3, ϕ = 64.8° and α = 30°. For this run, individual post-processing was performed for subsets of image pairs in multiples of 100, from 100 to 700 image pairs and average velocity fields were obtained for each of those subsets. The relative differences between those average fields and the one obtained from 1400 image pairs were computed and shown in Fig. 3.1 for a few subsets of image pairs. For the 700 image pairs, a standard error below 0.02 V_{1400} was observed in regions not affected by wall effects. This ±2% difference from the 1400 image pairs averaged velocity was considered acceptable since it is lower than the mean standard deviation across the flow field.

The 700 image pairs were considered a good representative set of the flow field and further image processing was not needed for subsequent data sets. To obtain a better convergence on the average fields, instantaneous velocity fields that were above two standard deviations of the average of 700 image pairs were considered as outliers and removed from the average field (Fig. 3.2). For each run, this resulted in a slightly different number of instantaneous fields being considered as part of the average. All phase-averaged fields in section 3.1.1 were obtained as a result of this process, with a range of 635 to 699 instantaneous image pairs.

3.1.2 Baseline Flow and Phase Averaged Fields

Phase-averaged velocity fields were obtained for the investigated oscillating jet in crossflow. The baseline case with no blowing (Fig. 3.3) shows a growing boundary layer which remains fully attached along the streamwise direction. Characterizing the flow field produced without surface

blowing allows influences of the blowing ratios on such boundary layer to be captured across the jet oscillation cycles.

The instantaneous vectors fields for each streamwise plane were obtained using the methods outlined in Section 2.3.4 and the average velocity fields were determined for each phase angle for the 30° inclination angle. The phase-averaged velocity fields are presented in Fig. 3.4 for BR = 3 across the center plane of the oscillator outlet. Across this one period of the oscillation, these flow fields reveal that the jet mostly resides across the center plane at a phase angle of 64.8°. The curvature of the streamlines also appears to be greatest across the center plane for this phase angle. These phase-averaged center plane results are consistent with the three-dimensional flow field presented later (Fig. 3.11) and the phase angle with dominant flow structure appears to have the most wall-normal jet penetration across the center plane.

The phase-averaged velocity fields across the actuator center plane for BR = 5 are presented in Fig. 3.5 for all eight phase angles. At a phase angle of 68.4°, the jet is more pronounced along the center plane compared to other phase angles due to the alignment of the jet with the freestream along the oscillator centerline. This phase angle is similar to the one for BR = 3. The jet velocity at this phase angle is observed to retain higher velocity magnitudes further away from the wall while slower velocity regions are located closer to the wall. This suggests that the low velocity regions of fluid are being pulled away from the wall by a larger vortex created at the higher blowing ratio, or due to a greater extent of mixing created at the higher blowing ratio. For BR = 7, the observed bi-stable jet deflection across the oscillator centerline is slightly different from the BR = 3 and BR = 5 cases, where higher jet velocities are observed for ϕ = 64.8°and ϕ = 68.4°, respectively, due to the difference in jet oscillation frequency. For this higher BR, the jet seems to dwell at the center plane at a phase angle of ϕ = 118.8°. Compared to the BR = 3 case, entrainment of slower regions away from the wall is also observed. However, those lower velocity regions are smaller compared to the BR = 5 case, due to the higher momentum injected at BR = 7.

In addition to the previous observations, the phase-averaged velocity fields at the center plane (Fig. 3.4, Fig. 3.5 and Fig. 3.6) show higher velocity gradients in the near field of the oscillator outlet for BR = 7, with streamlines bending further away from the wall in the vicinity of the oscillator outlet. The extent of the wall-normal jet penetration across the three blowing ratios is shown at the center plane for selected phase angles (Fig. 3.7). Around the jet outlet, the wall-normal penetration of the jet produced by the BR = 3 case slowly increases with further streamwise

distance, as compared to the BR = 5 and BR = 7 cases. However, for all BR cases, most wall-normal jet penetration happens further downstream of the oscillator outlet location. As expected, the streamlines for the higher blowing ratios bend further away from the wall along the entire FOV, resulting in jet wall-normal penetration heights up to 51mm for BR = 5 and 58 mm for BR =7.

To quantify the influence of the inclination angle on the boundary layer, the phase averaged velocity fields were obtained at $\alpha = 30°$, $\alpha = 60°$, and $\alpha = 90°$ for two fixed conditions BR = 3, $\phi = 64.8°$ and BR = 5, $\phi = 68.4°$ (Fig. 3.8 and Fig. 3.9). For $\alpha = 30°$, as observed previously, the jet flow remains primarily attached to the wall surface and produces a region of high-momentum flow within the boundary-layer region for BR = 3. Furthermore, entrainment of low-momentum fluid away from the wall is observed for the higher blowing ratio. For $\alpha = 60°$, the curvature of the streamlines become more pronounced in the entire flow field downstream of the oscillator outlet compared to $\alpha = 30°$ case. A visibly higher wall-normal penetration also occurs. For BR = 3 however, the boundary layer is mainly influenced by the addition of momentum in the near field of the oscillator outlet. At the higher blowing ratio, the injection of momentum into the boundary layer also occurs further downstream, as seen through the higher curvature of the streamlines into the boundary layer between 90 and 110 mm (Fig. 3.9). For $\alpha = 90°$, the jet affects the entire flow field above the oscillator outlet (Fig. 3.8). The influence of the jet on the boundary layer is also localized to within the immediate surroundings of the oscillator outlet. For BR = 5, the trajectory of the jet within the surrounding flow field becomes more defined and momentum is also injected into the boundary layer further away from the oscillator outlet. The effect of these inclination angles on the jet penetration extent are shown in Fig. 3.10 for the BR = 3 and $\phi = 64.8°$ condition. Wall-normal penetration heights of up to 76 mm and 78 mm appear for $\alpha = 60°$ and $\alpha = 90°$, respectively. The overall penetration for $\alpha = 60°$ and $\alpha = 90°$, is higher compared to $\alpha = 30°$ along the streamwise direction. However, the wall-normal penetration for $\alpha = 90°$ becomes smaller compared to $\alpha = 60°$ after x = 85.24 mm. For this inclination angle, the jet is normal to the crossflow and its features are not carried as far downstream.

3.1.3 Three-Dimensional Velocity Isosurfaces

For $\alpha = 30°$, isosurfaces of velocity are shown in Fig. 3.11, Fig. 3.12 and Fig. 3.13 for BR = 3, BR = 5 and BR = 7, respectively, across a half oscillation cycle. For all BRs, high-momentum

regions form across the half oscillation cycle and convect downstream of the oscillator outlet. For BR = 3, more of the low-velocity regions are located in the near field of the oscillator exit and remain close to the wall while higher velocity regions propagate further downstream. At $\phi = 64.8°$, a high velocity region, which propagates further into the spanwise direction and downstream compared to the other phase angles, is visible. Observation of further lateral spreading of the jet at those other phase angles is limited by the sPIV resolution in the spanwise direction. At $\phi = 64.8°$, the jet exits the outlet right along the oscillator centerline, leading to a further downstream convection of higher momentum regions at phase angles that align with the midplane of the oscillator outlet.

At the higher BR = 5 case, an increase in spanwise spreading of the jet is observed for a half oscillation cycle (Fig. 3.12). In this case, larger regions of both high and low velocities exist in the far field of the jet exit, with higher momentum regions engulfing the lower momentum regions. For the BR = 5 case, the jet momentum is not only convected downstream, but it is also carried further into the wall-normal direction, following the streamlines. Correspondingly, the largest jet deflection is observed for a similar phase angle to that of BR = 3, at $\phi = 68.4°$. For the BR = 7 case, regions of low momentum are localized and mainly confined to the near-wall region, with no high-momentum regions enveloping low-momentum ones downstream of the oscillator outlet (Fig. 3.13). For this case, there is a further lateral spreading of the jet for all phase angles across the oscillator outlet. However, the highest wall-normal penetration occurred at a phase angle around $\phi = 208.8°$. This discrepancy in phase angle is due to the difference in jet oscillation frequency between BR = 3, BR = 5 and BR = 7, and potential intrinsic delays in the phased-locking trigger system. From these isosurfaces, a similar pattern, in terms of high momentum and low momentum regions, emerged between BR = 3, BR = 5 and BR = 7 cases for similar phase angles investigated (Fig. 3.11, Fig. 3.12 and Fig. 3.13).

For $\alpha = 60°$ and $\alpha = 90°$, the isosurfaces of velocity are obtained for a fixed BR = 3 and $\phi = 64.8°$ (Fig. 3.14). Similar to $\alpha = 30°$, the entrainment of low-momentum regions is localized for this blowing ratio and phase angle condition. However, the high-momentum regions are pushed further away from the wall with increased inclination angle. For $\alpha = 60°$, the alignment of the jet with crossflow at this phase angle promote the downstream propagation of the jet. Two high-momentum lobes, which do not propagate to the far field, emerge at $\alpha = 90°$. This is due to the normal jet direction relative to the crossflow. A higher crossflow velocity would be needed to carry

those high-momentum regions as far downstream as for α = 30° and α = 60°. Another fixed condition with BR = 5 and ϕ = 64.8° was investigated for α = 60° and α = 90° (Fig. 3.15). At this higher blowing ratio, more lateral spreading and higher wall-normal penetration is observed for both inclination angles. The low-momentum regions were also pushed further away from the wall but without being entrained by the high momentum regions as seen in the case when α = 30°. For α = 90°, the high momentum lobes became more defined on either side of the oscillator center plane at the higher blowing ratio. The inclination angle α = 60° seemed to have more wall normal penetration for both blowing ratios considered, with penetration heights of almost double that of the jet inclined at α = 30°.

3.2 Vortex Identification

3.2.1 Three-Dimensional Q-criterion Isosurfaces

The three-dimensional flow field across the oscillator exit was obtained for each phase angle and the dominant coherent structures were subsequently extracted. Isosurfaces of Q-criterion were plotted to identify coherent vortex structures in the flow. The Q-criterion, which is an Eulerian vortex identification method, defines a comparison between local rotation rate and local stretching in the flow. Hunt et al. [12] identified eddies as regions with a positive value of the Q-criterion (Eq. 3.1), for which the Euclidean norm of the vorticity tensor is greater than that of the strain rate tensor.

$$Q = \frac{1}{2}\left(||\Omega||^2 - ||S||^2 \right) > 0 \tag{3.1}$$

where $\Omega = \Omega_{ij} = \frac{1}{2}\left(\frac{\partial u_j}{\partial x_i} - \frac{\partial u_i}{\partial x_j}\right)$ is the vorticity tensor and $S = S_{ij} = \frac{1}{2}\left(\frac{\partial u_j}{\partial x_i} + \frac{\partial u_i}{\partial x_j}\right)$ is the strain rate tensor. For the three-dimensional flow field, equation 3.1 reduces to

$$Q = -\frac{1}{2}\left(\frac{\partial u_j}{\partial x_i}\frac{\partial u_i}{\partial x_j}\right) = -\frac{1}{2}\left(\frac{\partial u}{\partial x}^2 + \frac{\partial v}{\partial y}^2 + \frac{\partial w}{\partial z}^2\right) - \frac{\partial u}{\partial y}\frac{\partial v}{\partial x} - \frac{\partial u}{\partial z}\frac{\partial w}{\partial x} - \frac{\partial v}{\partial z}\frac{\partial w}{\partial y} \tag{3.2}$$

The flow is assumed to be solenoidal in equation 3.2, which can be applied to the considered flow velocities, as the investigated blowing ratios produce jet velocities below Mach 0.3.

Across the full oscillation cycle, the formation of downstream-propagating vortices is observed for α = 30°. For BR = 3, a main vortex structure moving through the oscillation period

is identified. The Q-criterion isosurfaces colored by streamwise vorticity are shown in Fig. 3.16 at the two-phase angles for which dominant structures are identified across a full oscillation cycle. A large vortex forms at $\phi = 64.8°$ as the jet moves in the -z direction and slowly dissipates into weaker structures before starting a stroke in the +z direction. The formation of another dominant vortex begins as the jet continues its upstroke. The newly formed vortex entrains fluid further downstream and is located at $\phi = 244.8°$. As the vortex moves further across the oscillator exit, the structure is less defined and shrinks before a new jet trajectory starts in the -z direction. These predominant phase angles, for which the vortices are more defined, are 180° out of phase. The main vortices possess opposite streamwise vorticity signs which is expected as the jet moves across a full oscillation and changes direction. The further downstream propagation of the jet, observed at $\phi = 244.8°$, suggests that the jet characteristics are not identically symmetric across the oscillator centerline, due to limitations in the manufacturing tolerances. Three-dimensional isosurfaces of Q-criterion are also shown for phase angles across a half oscillation cycle (Fig. 3.17). These show that as the jet moves across the half oscillation cycle and the dominant vortex structure becomes smaller, a new vortex of opposite sign start to emerge alongside the first vortex residual, forming a pair of counterrotating vortices. The former vortex is carried further downstream as the new one emerges and grows while the jet is about to begin a second half oscillation. Those pairs are present for phase angles at which the jet does not align with the extremities of the oscillator outlet. The strongest vortical structure across this half oscillation cycle also corresponded to $\phi = 64.8°$ for BR = 3.

For BR = 5, a similar formation of vortices across half an oscillation cycle is also observed (Fig. 3.18). For this case, a larger second vortex with positive vorticity emerges as the jet moves across the half oscillation cycle. The higher oscillation frequency prevents that secondary vortex from dissipating as rapidly as in the BR = 3 case, promoting the wall-normal entrainment of fluid observed in the phase-averaged fields. In addition to that, larger lateral deflections of the vortices occur throughout the oscillation cycle. The lateral spreading of the jet seen in the velocity isosurfaces at this blowing ratio was accompanied with the formation of larger vortex cores and promoted the deflection of the vortices and mixing of the flow along the span of the oscillator outlet. For BR = 7, the vortex pairs are still present but are less pronounced for the studied phase angles (Fig. 3.19). These phase angles are similar to the ones across BR = 3 and BR = 5, but not exactly the same. The phase angles captured for BR = 7 show the behavior of vortices at different

intermediate locations across the oscillation cycle. The lateral deflection of the vortices is larger and present at more phase angles. This is due to the larger momentum input at the blowing ratio of 7.

The vortex formation process appears to be different for $\alpha = 60°$ and $\alpha = 90°$ (Fig. 3.20). For $\alpha = 60°$, the emergence of a vortex with opposite vorticity is more visible at $\phi = 64.8°$. This second vortex is located above the one with negative vorticity. At this inclination angle, the residuals of previous vortices are not only propagated downstream across phase angles, but they are also pushed away from the wall, leading to the formation of vortex "stacks" at different phase angles. At $\alpha = 90°$, a series of less coherent vortices with weaker cores form in the near field of the oscillator outlet (Fig. 3.20). The dominant vortices at $\phi = 64.8°$ have vorticity signs that are opposite to the main vortex structure observed for $\alpha = 30°$. This feature is produced due to the obstruction to the crossflow caused by the normally inclined jet. Shear layer vortices roll up against the crossflow with higher spanwise vorticity, reducing the overall strength of the streamwise vortices at $\alpha = 90°$. For the higher blowing ratio BR = 5, isosurfaces of Q-criterion colored by streamwise vorticity are shown in Fig. 3.21 for $\alpha = 60°$ and $\alpha = 90°$. The vortices appear to form in a similar manner as for BR = 3. However, for $\alpha = 60°$, a residual vortex pair with positive vorticity appear to form above a pair of vortices with negative vorticity. For both $\alpha = 60°$ and $\alpha =$ 90, the vortices are propagated further downstream and affect larger areas with less concentration of vorticity and decreased coherence of vortex structures.

3.3 Turbulence Statistics

The oscillating nature of jet injected into the boundary creates turbulence within the flow. For the 30° inclination, the contribution of the turbulent fluctuations to the mean motion of the flow field can be quantified through Reynolds stresses and the turbulent kinetic energy. For the phase-averaged sPIV results, the turbulence spectrum is assumed to have reached steady state in order to be considered as fully developed turbulence while computing turbulence statistics.

3.3.1 Reynolds Stresses

The Reynolds normal stresses, R_{xx} and the Reynolds shear stresses R_{xy} and R_{zy} were obtained according to the following equations:

$$R_{xy} = \overline{u'v'} \tag{3.3}$$

$$R_{xx} = \overline{u'^2} \tag{3.4}$$

$$R_{zy} = \overline{v'w'} \tag{3.5}$$

where u', v' and w' are the x, y and z components of velocity fluctuations from the mean, respectively. Additional Reynolds shear stress components were not presented in this study while the remaining Reynolds normal stresses are included in the turbulent kinetic energy.

The turbulent shear stress across the streamwise-wall-normal plane is quantified through R_{xy}. For BR = 3, the R_{xy} Reynolds stress components are shown across phase angles for half of an oscillation cycle phase angles in Fig. 3.22. Positive and negative regions of R_{xy}, which coincide with vortical regions observed for BR = 3, appear to be the main driving factor behind the formation of the vortices across the oscillation cycle, as the regions of strongest shear stress are observed near the cores of the coherent vortex structures identified previously. The R_{xx} components reveal the streamwise momentum fluxes due to u' through faces normal to the streamwise direction (Fig. 3.23). The R_{xx} normal stresses have similar features to the velocity isosurfaces and drive the streamwise propagation of the jet. The regions of low velocity (Fig. 3.11) correspond to low R_{xx} regions while higher momentum regions corresponding to high R_{xx} regions. The R_{zy} shear stresses quantify the contribution of w'velocity fluctuations due to the oscillatory nature of the jet. These mainly effect the wall-normal penetration and the lateral spreading of the jet. The overall structure is similar to the isosurfaces of velocity (Fig. 3.24), following the jet deflection pattern. For phase angles at which the jet is aligned with the centerline of the oscillator, higher R_{zy} regions are located near the oscillator outlet. For other phase angles, the corresponding maximum Reynolds shear stress regions are located in the far field of the oscillator outlet.

Fig. 3.26 and Fig. 3.27 show the Reynolds normal and shear stresses along with the turbulent kinetic energy at a given phase angle for BR = 5 and BR = 7, respectively. For both BR = 5 and BR = 7, the R_{xy} Reynolds stress components contribute less to the formation of the vortex pairs compared to the BR = 3 case for which R_{xy} contributes more to the smaller and stronger vortices. Regions of positive and negative R_{xy} only overlap partially with vortex cores obtained at BR = 5 and BR = 7, leading to larger and weaker vortices generated at those blowing ratios. The R_{zy} shear stresses for both BR = 5 and BR = 7 also follow the jet wall-normal and lateral deflection patterns seen in the three-dimensional velocity isosurfaces. These shear stresses contribute to more wall-normal jet penetration as the blowing ratios increase.

For BR = 5, the normal shear stress R_{xx} contributes the most to the downstream propagation of the jet. As seen in Fig. 3.26, regions of low R_{xx} correspond to the engulfed low momentum regions shown in the velocity isosurfaces while high R_{xx} regions match with high momentum regions. For BR = 7, larger R_{xx} regions are observed further downstream of the oscillator outlet (Fig. 3.27). There is enough momentum addition that low R_{xx} regions are barely present, which is consistent with the phase-averaged fields and the three-dimensional velocity isosurfaces.

3.3.2 Turbulent kinetic energy

In addition to the different components of Reynolds stresses, the turbulent kinetic energy (Eq. 3.6) was obtained to quantify the overall turbulence level in the flow field.

$$TKE = \frac{1}{2}\left(\overline{u'^2} + \overline{v'^2} + \overline{w'^2}\right) \tag{3.6}$$

For BR = 3, the turbulence intensity (TKE) across a half oscillation cycle is shown in Fig. 3.25. Higher TKE regions are located in the near field of the oscillator outlet for phase angles at which the jet is aligned with the crossflow. The maximum TKE location is then propagated downstream as the jet passes through other phase angles. Across the oscillation cycle, the unsteady turbulent motion of the jet is captured through the TKE and contributes to wall-normal and lateral deflection of the jet at each phase angle. For BR = 5, the low TKE regions also correspond to low-momentum cores seen in the velocity isosurfaces. For both BR = 5 and BR = 7, most of the turbulent influences are concentrated in the far field of the oscillator outlet as shown for (Fig. 3.26 and Fig. 3.27). The overall TKE increases with increased blowing ratio.

3.4 Chapter 3 Figures

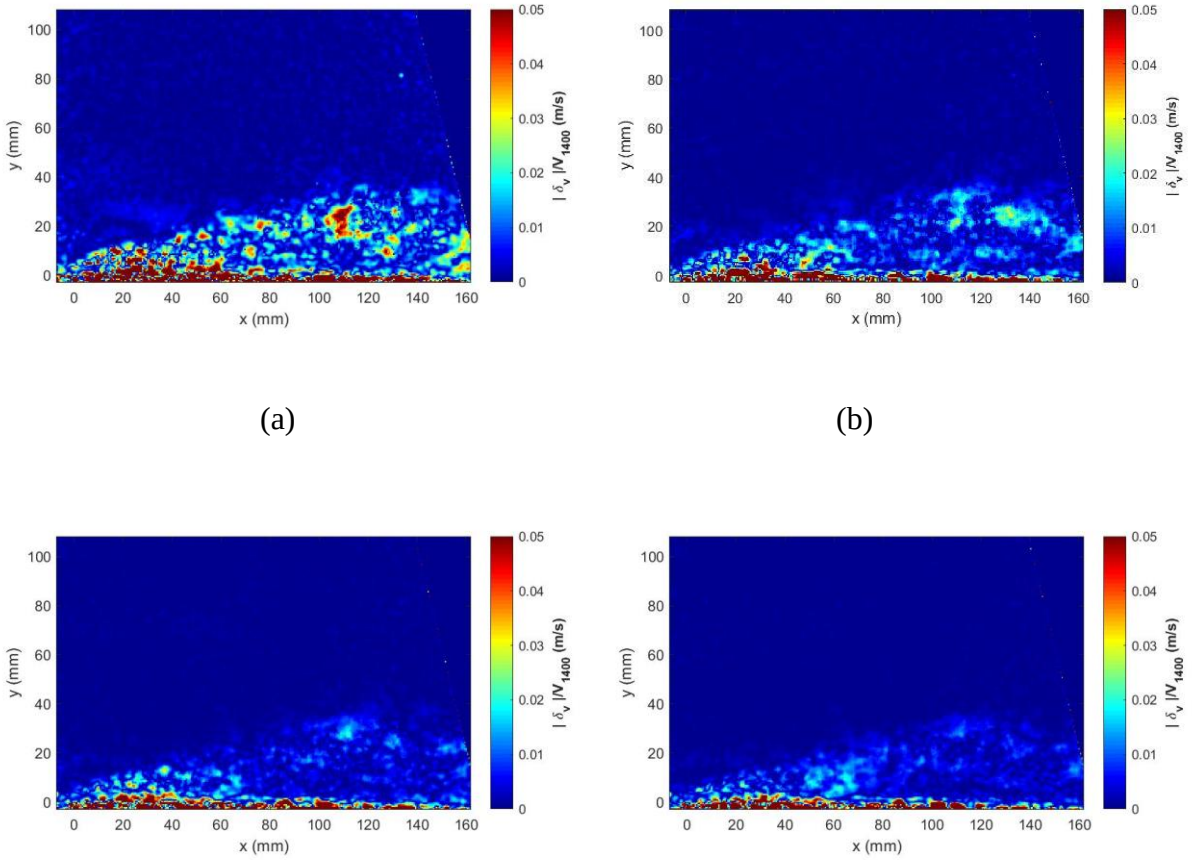

Fig. 3.1 Relative mean difference for (a) 100 image pairs, (b) 300 image pairs, (c) 500 image pairs and (d) 700 image pairs

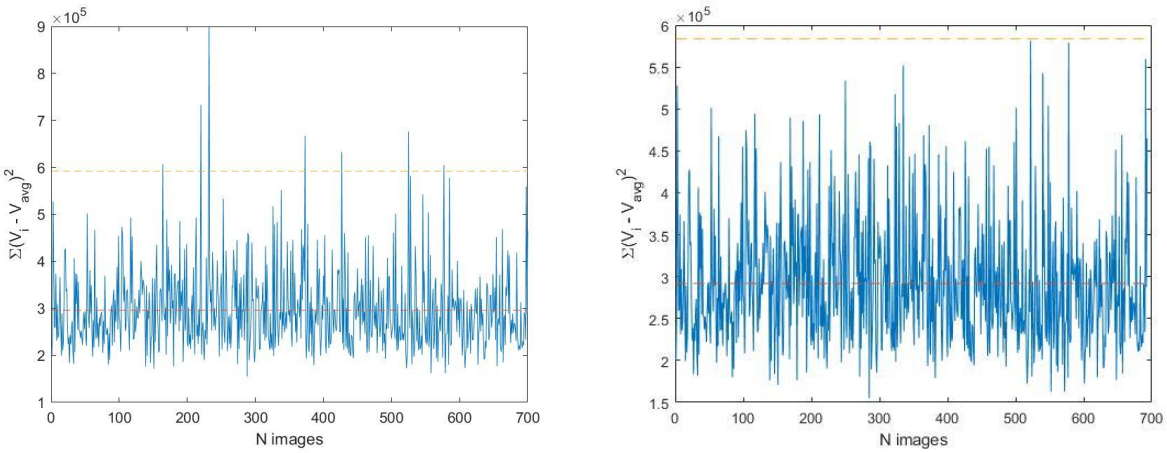

(a) (b)

Fig. 3.2 Absolute squared deviation of instantaneous images from average velocity field (a) with outliers, (b) without outliers

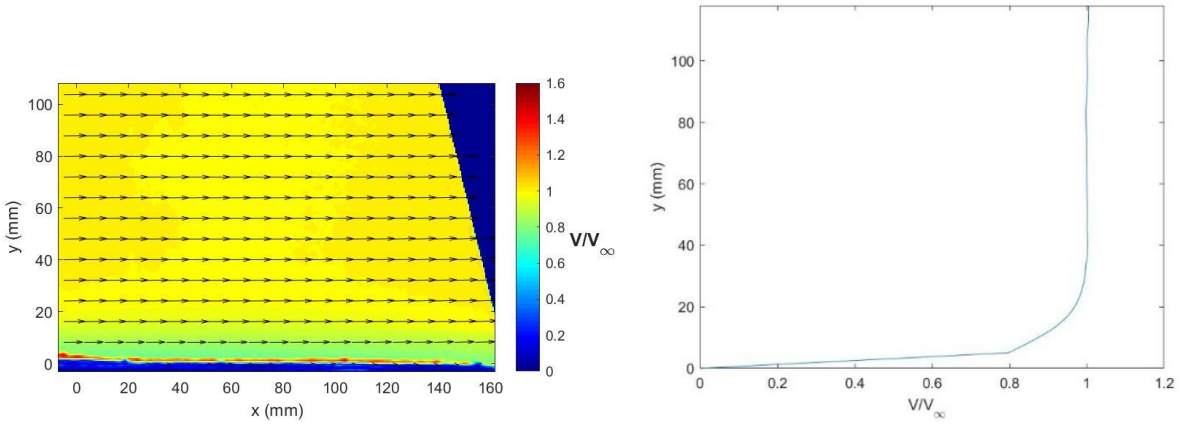

(a) (b)

Fig. 3.3 (a) Baseline average flow field velocity (b) Boundary Layer Profile at x = 45 mm

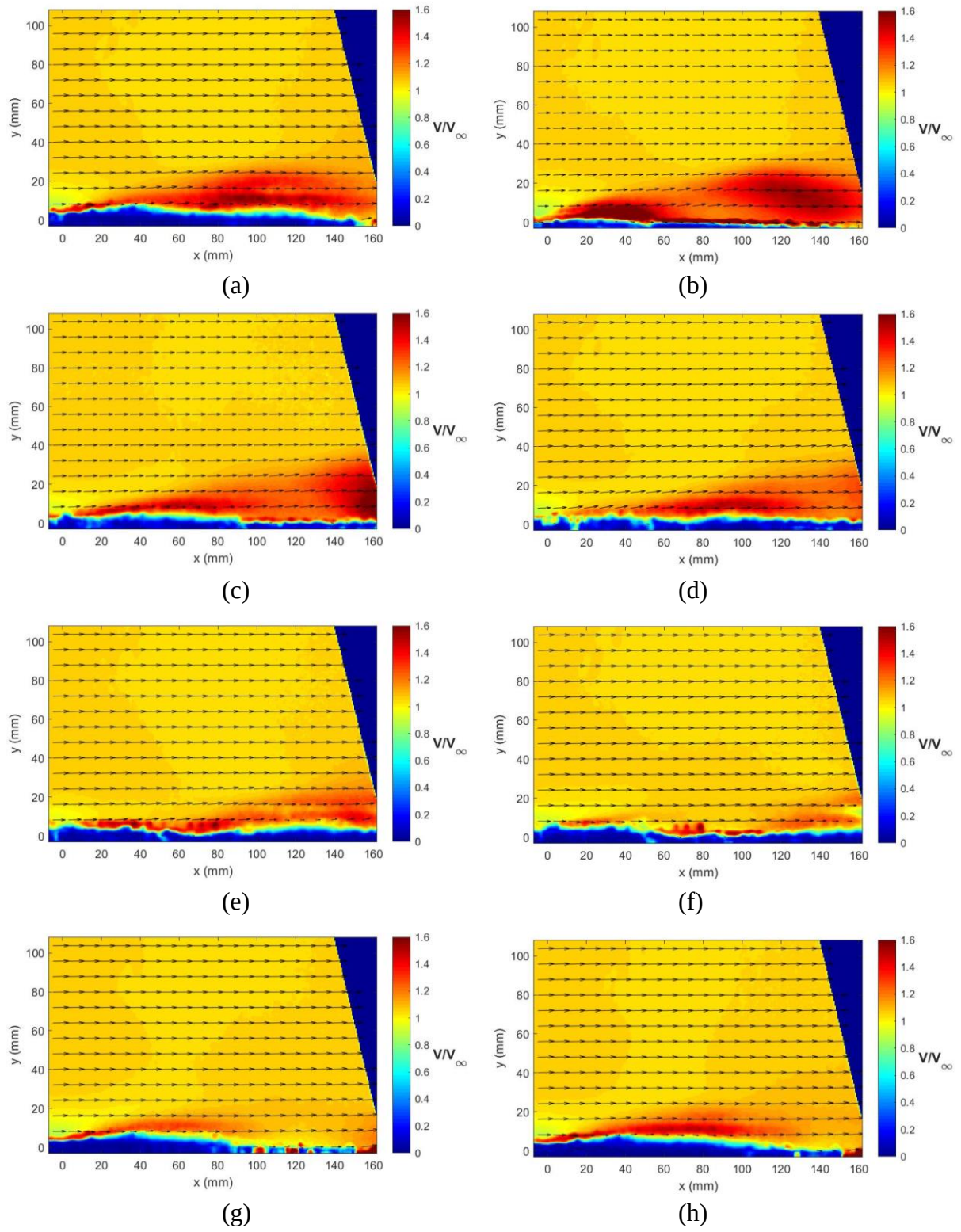

Fig. 3.4 Average velocity, V, for BR = 3 at center plane (a) ϕ = 19.8°, (b) ϕ = 64.8°, (c) ϕ = 109.8°, (d) ϕ = 154.8°, (e) ϕ = 199.8°, (f) ϕ = 244.8°, (g) ϕ = 289.8°and (h) ϕ = 334.8°.

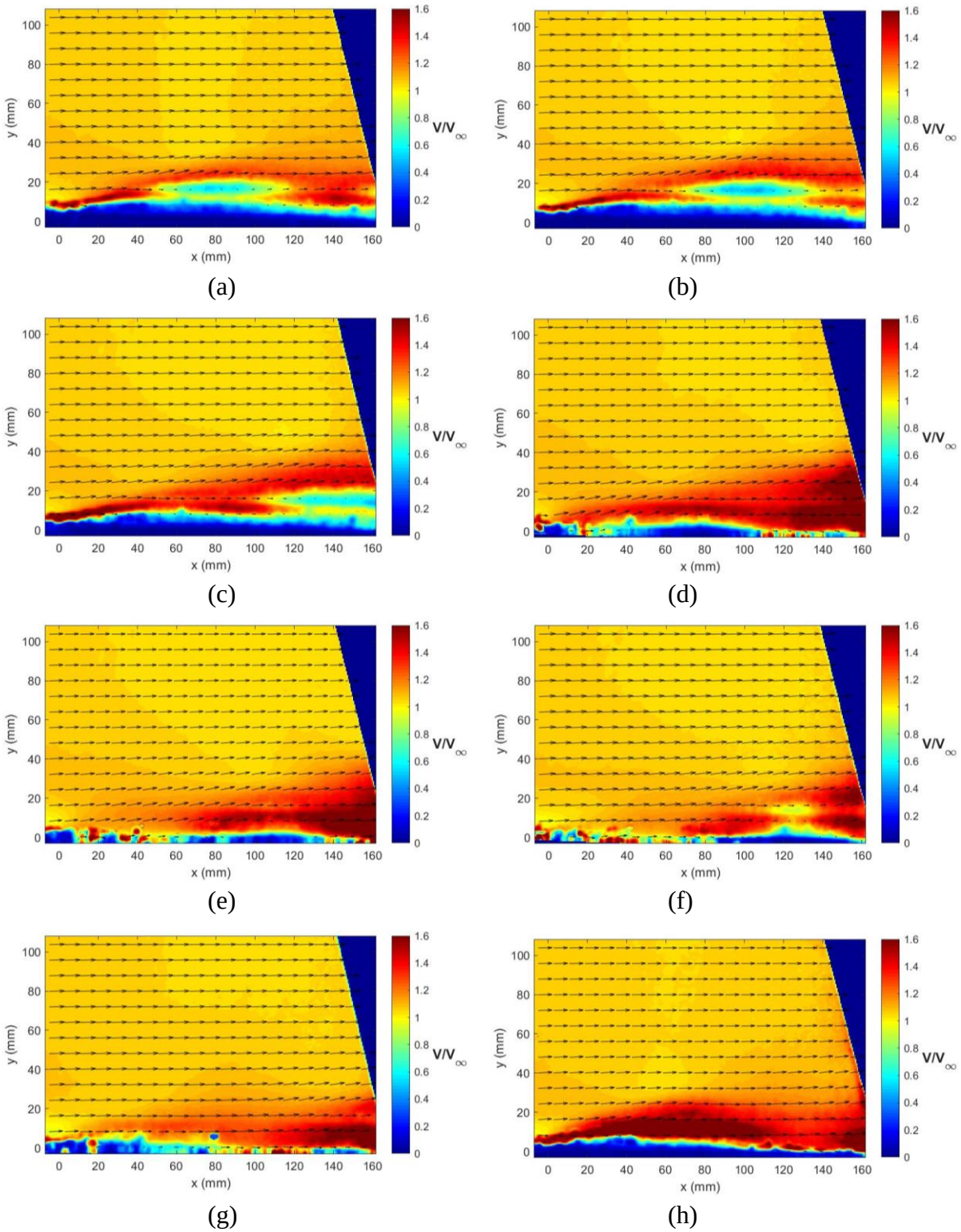

Fig. 3.5 Average velocity, V, for BR = 5 at center plane (a) ϕ = 23.4°, (b) ϕ = 68.4°, (c) ϕ = 113.4°, (d) ϕ = 158.4°, (e) ϕ = 203.4°, (f) ϕ = 248.4°, (g) ϕ = 293.4°and (h) ϕ = 338.4°.

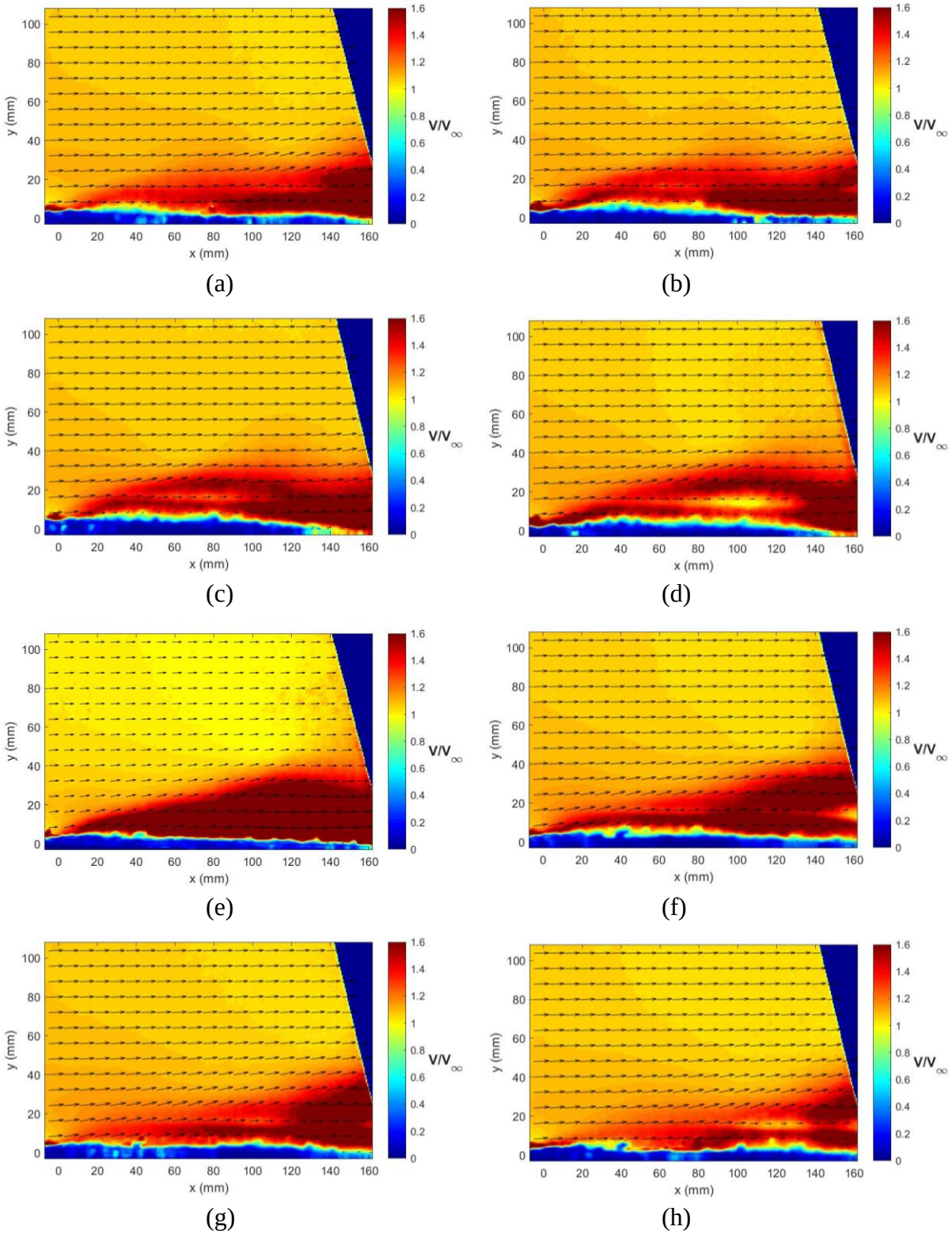

Fig. 3.6 Average velocity, V, for BR = 7 at center plane (a) ϕ = 28.8°, (b) ϕ = 73.8°, (c) ϕ = 118.8°, (d) ϕ = 163.8°, (e) ϕ = 208.8°, (f) ϕ = 253.8°, (g) ϕ = 298.8°and (h) ϕ = 343.8°.

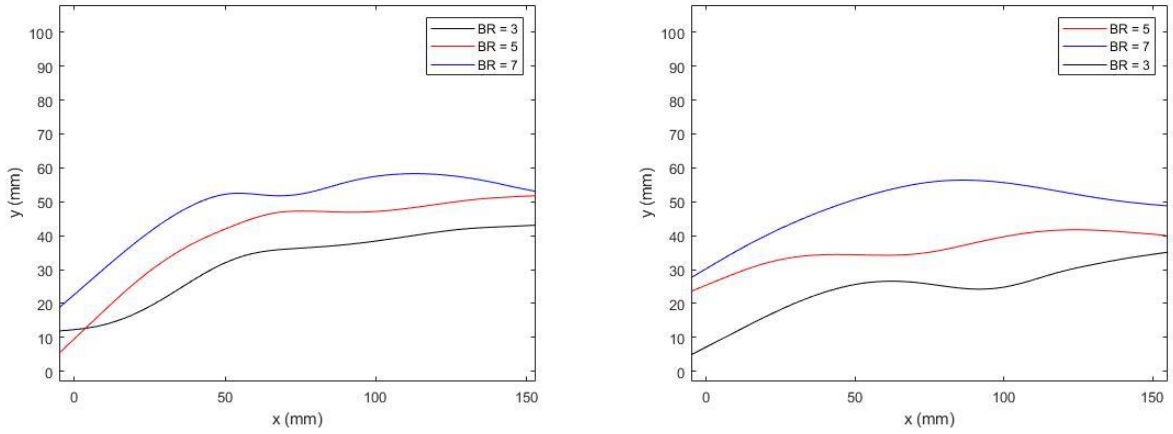

(a) (b)

Fig. 3.7 Wall normal penetration for (a) ϕ = 64.8° and BR = 3, ϕ = 68.4° and BR = 5, ϕ = 118.8° and BR = 7, (b) ϕ = 334.8° and BR = 3, ϕ = 338.4° and BR = 5, ϕ = 28.8° and BR = 7.

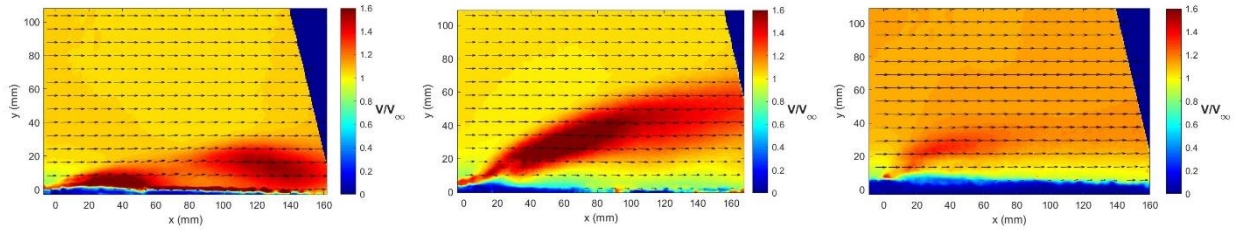

(a) (b) (c)

Fig. 3.8 Average velocity, V, for BR = 3, ϕ = 64.8° at center plane (a) α = 30°, (b) α = 60°, (c) α = 90°.

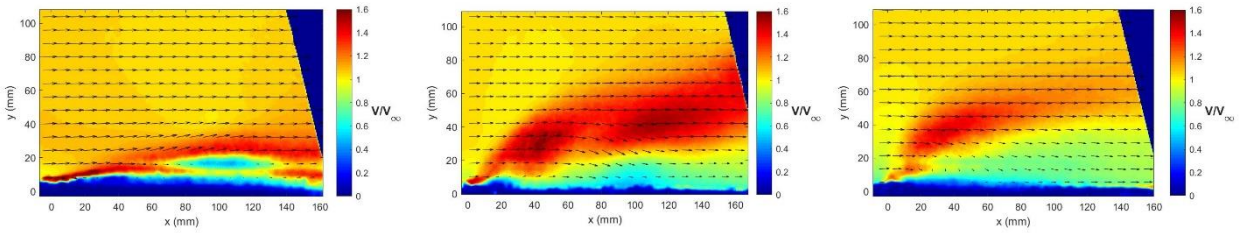

(a) (b) (c)

Fig. 3.9 Average velocity, V, for BR = 5, ϕ = 68.4° at center plane (a) α = 30°, (b) α = 60°, (c) α = 90°.

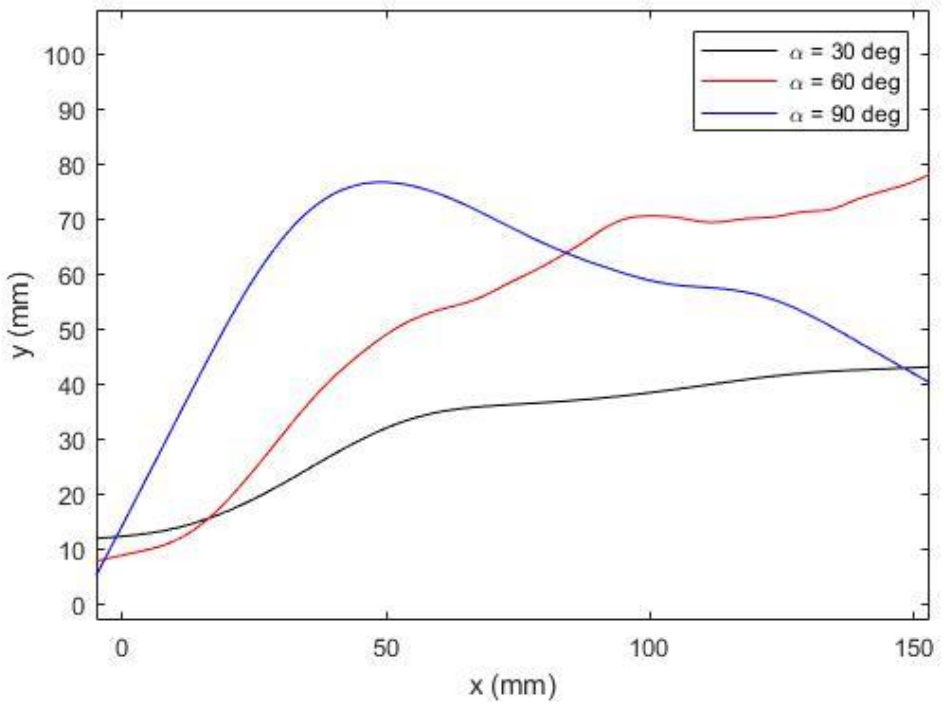

Fig. 3.10 Wall normal penetration for BR = 3, ϕ = 64.8° at different inclination angles.

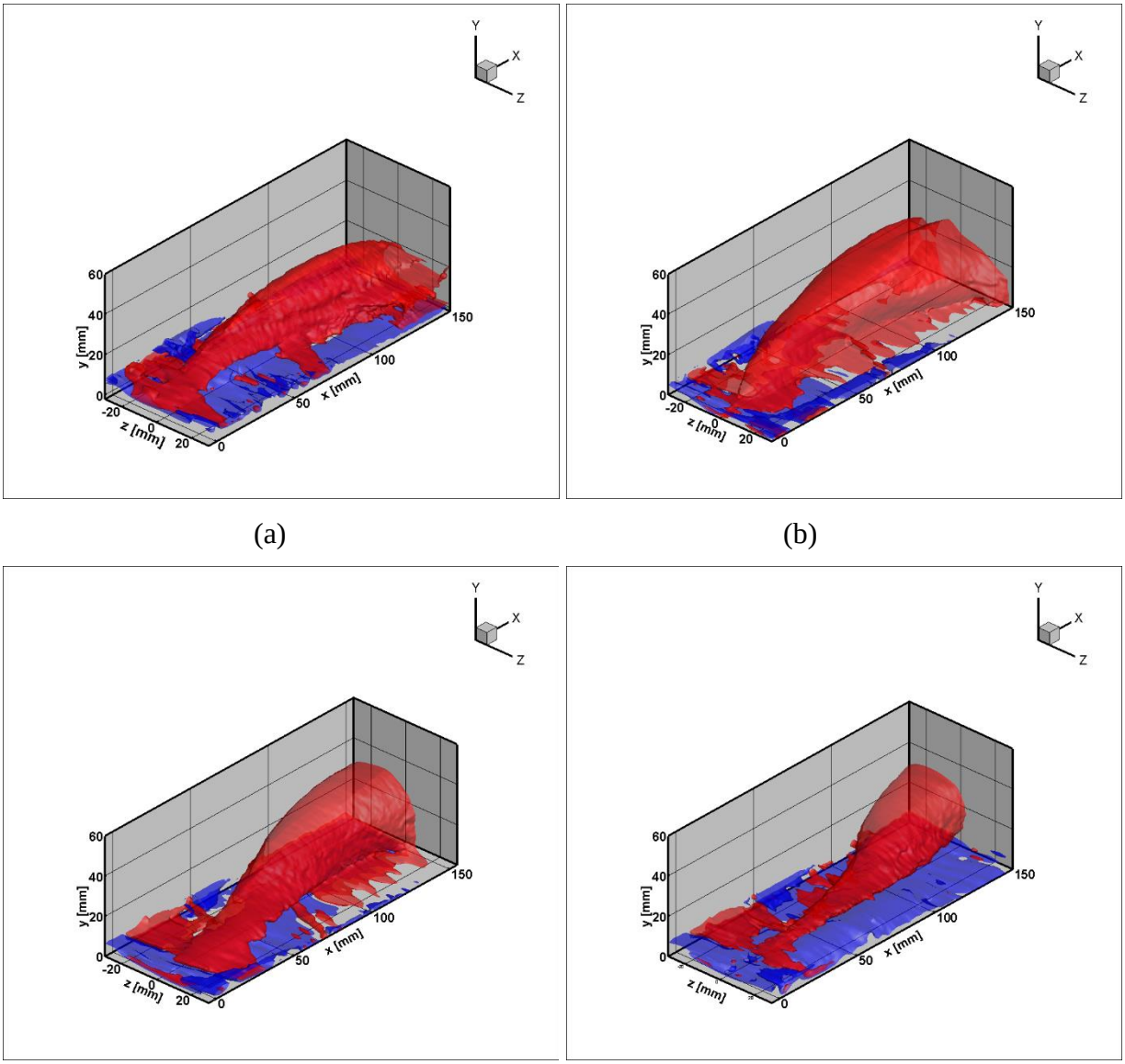

(a) (b)

(c) (d)

Fig. 3.11 Velocity isosurfaces across oscillator exit for BR = 3 and $U/U_\infty = 0.85$ (blue) and U/U_∞=1.2 (red) for a half oscillation (a) ϕ = 19.8°, (b) ϕ = 64.8°, (c) ϕ = 109.8°, (d) ϕ = 154.8°.

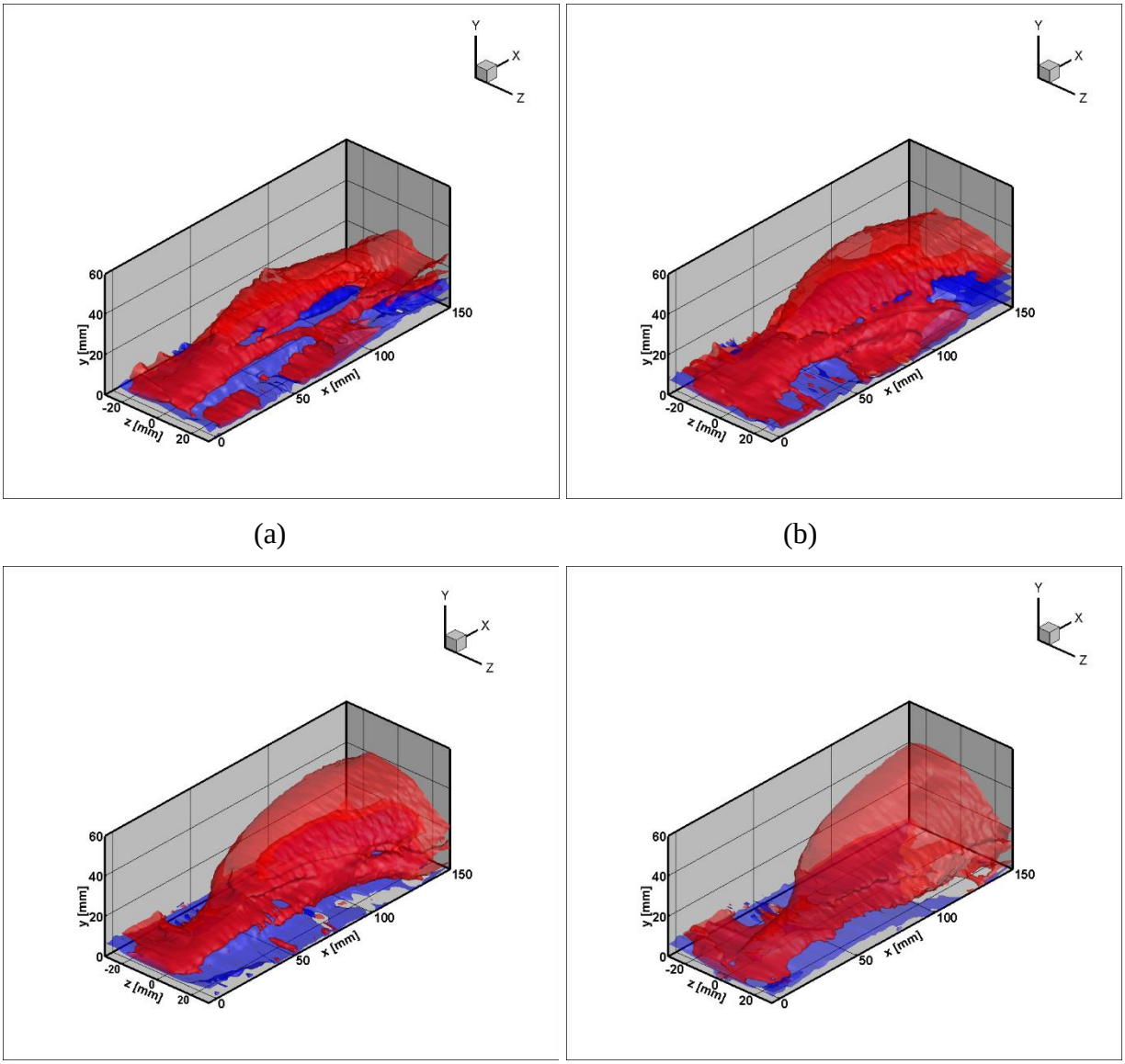

(a) (b)

(c) (d)

Fig. 3.12 Velocity isosurfaces across oscillator exit for BR = 5 and $U/U_\infty = 0.85$ (blue) and U/U_∞=1.2 (red) for a half oscillation (a) ϕ = 23.4°, (b) ϕ = 68.4°, (c) ϕ = 113.4°, (d) ϕ = 158.4°.

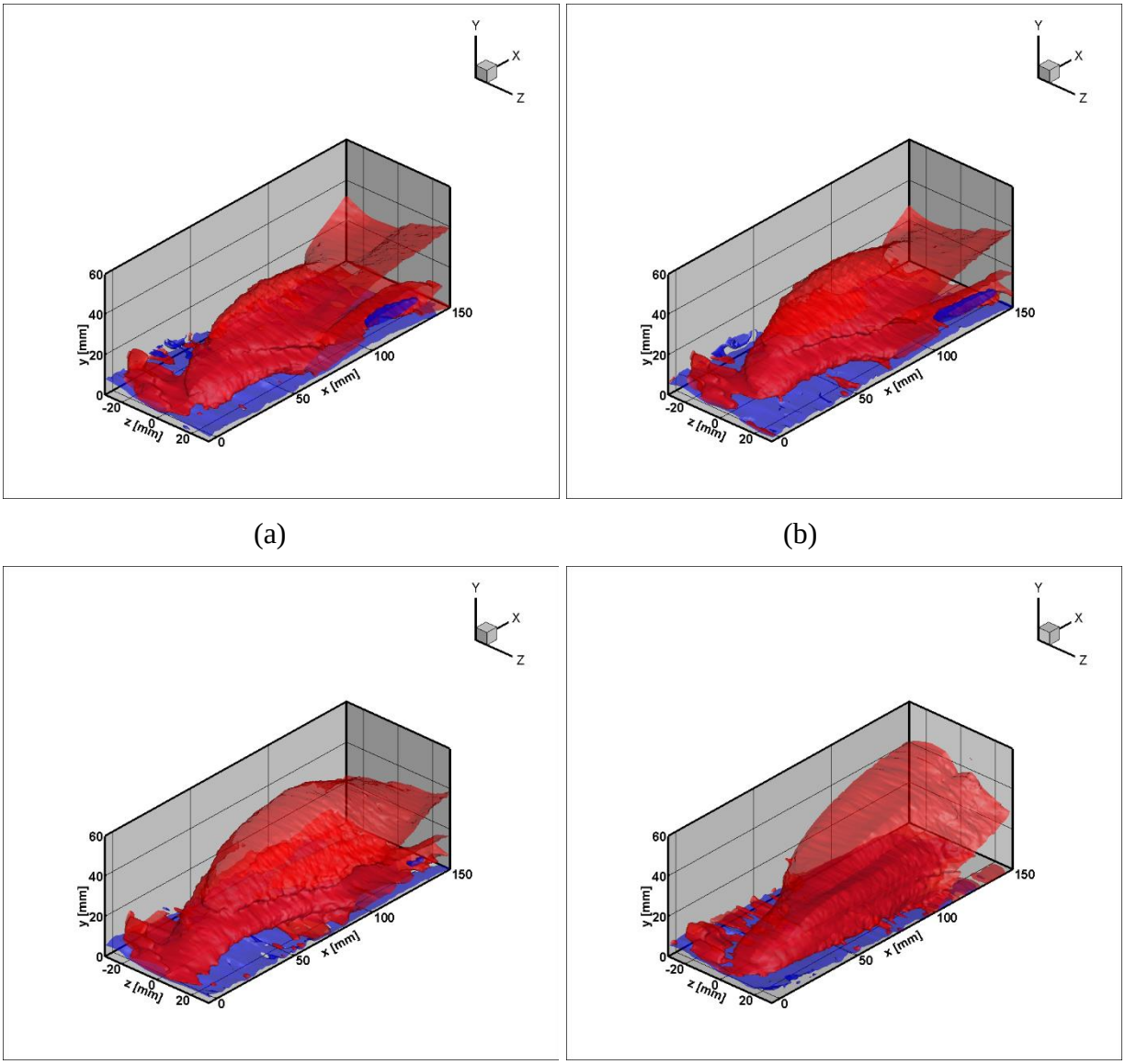

(a) (b)

(c) (d)

Fig. 3.13 Velocity isosurfaces across oscillator exit for BR = 7 and $U/U_\infty = 0.85$ (blue) and U/U_∞=1.3 (red) for a half oscillation (a) ϕ = 73.8°, (b) ϕ = 118.8°, (c) ϕ = 163.8°, (d) ϕ = 208.8°

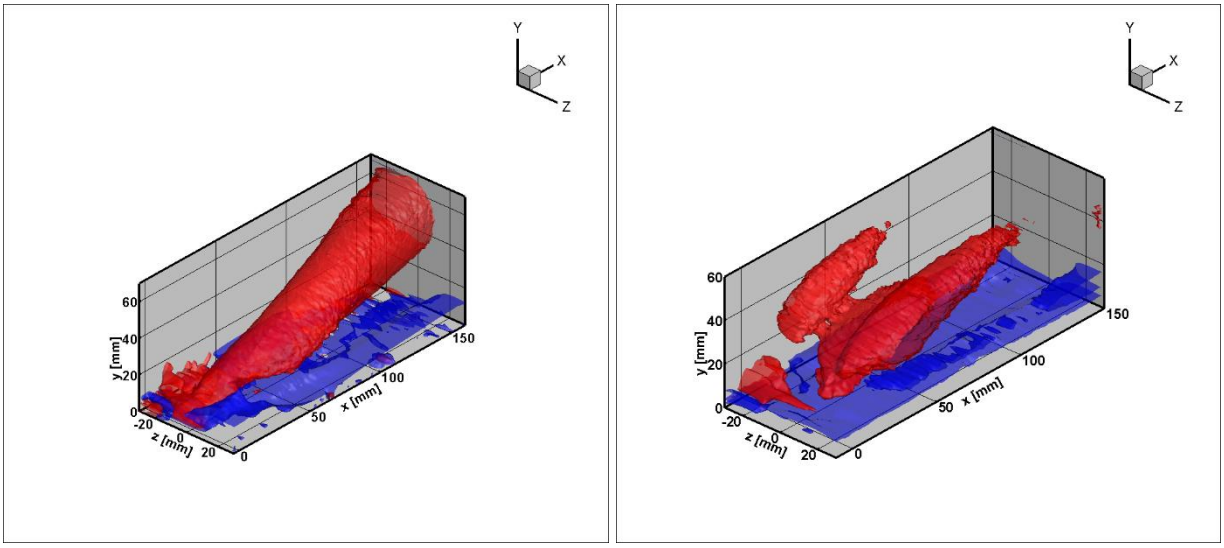

(a) (b)

Fig. 3.14 Velocity isosurfaces across oscillator exit for BR = 3, ϕ = 64.8°, $U/U_\infty = 0.85$ (blue) and U/U_∞=1.2 (red) and (a) α = 60°, (b) α = 90°.

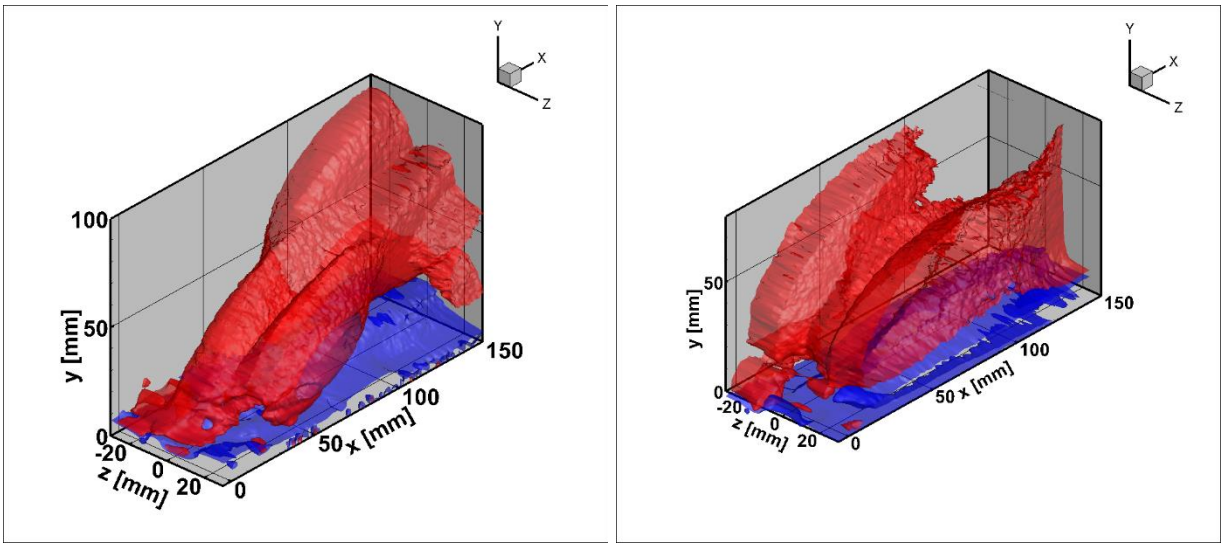

(a) (b)

Fig. 3.15 Velocity isosurfaces across oscillator exit for BR = 5, ϕ = 68.4°, $U/U_\infty = 0.85$ (blue) and U/U_∞=1.2 (red) and (a) α = 60°, (b) α = 90°.

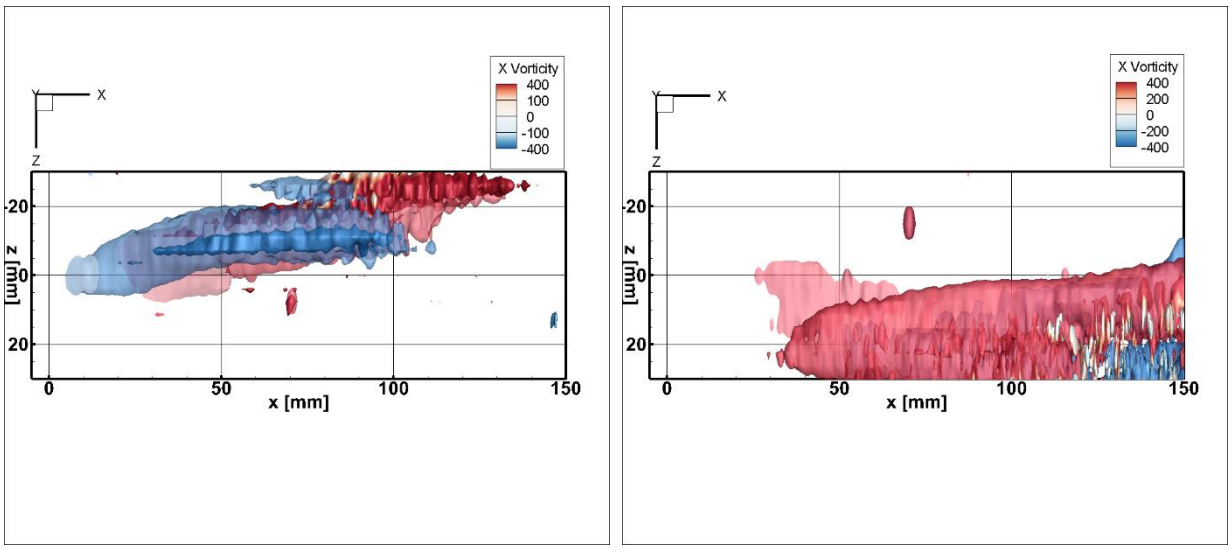

(a) (b)

Fig. 3.16 . Isosurfaces of Q colored by streamwise vorticity, ω_x, for BR= 3, (a) ϕ = 64.8° and (b) ϕ = 244.8° (top views).

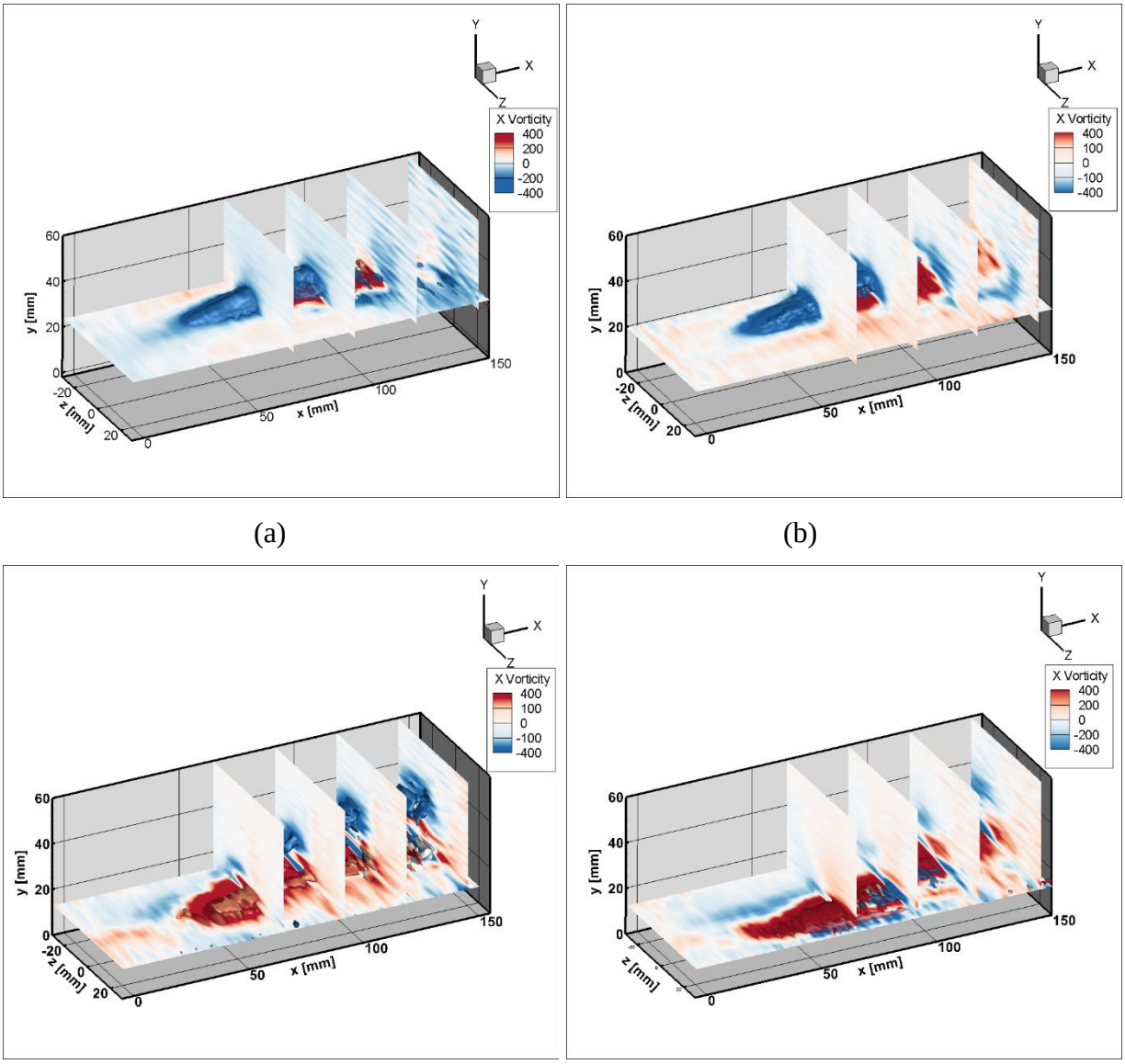

Fig. 3.17 Q-criterion isosurfaces colored by streamwise vorticity, ω_x, across a half oscillation for BR = 3 and (a) $\phi = 19.8°$, (b) $\phi = 64.8°$, (c) $\phi = 109.8°$, (d) $\phi = 145.8°$.

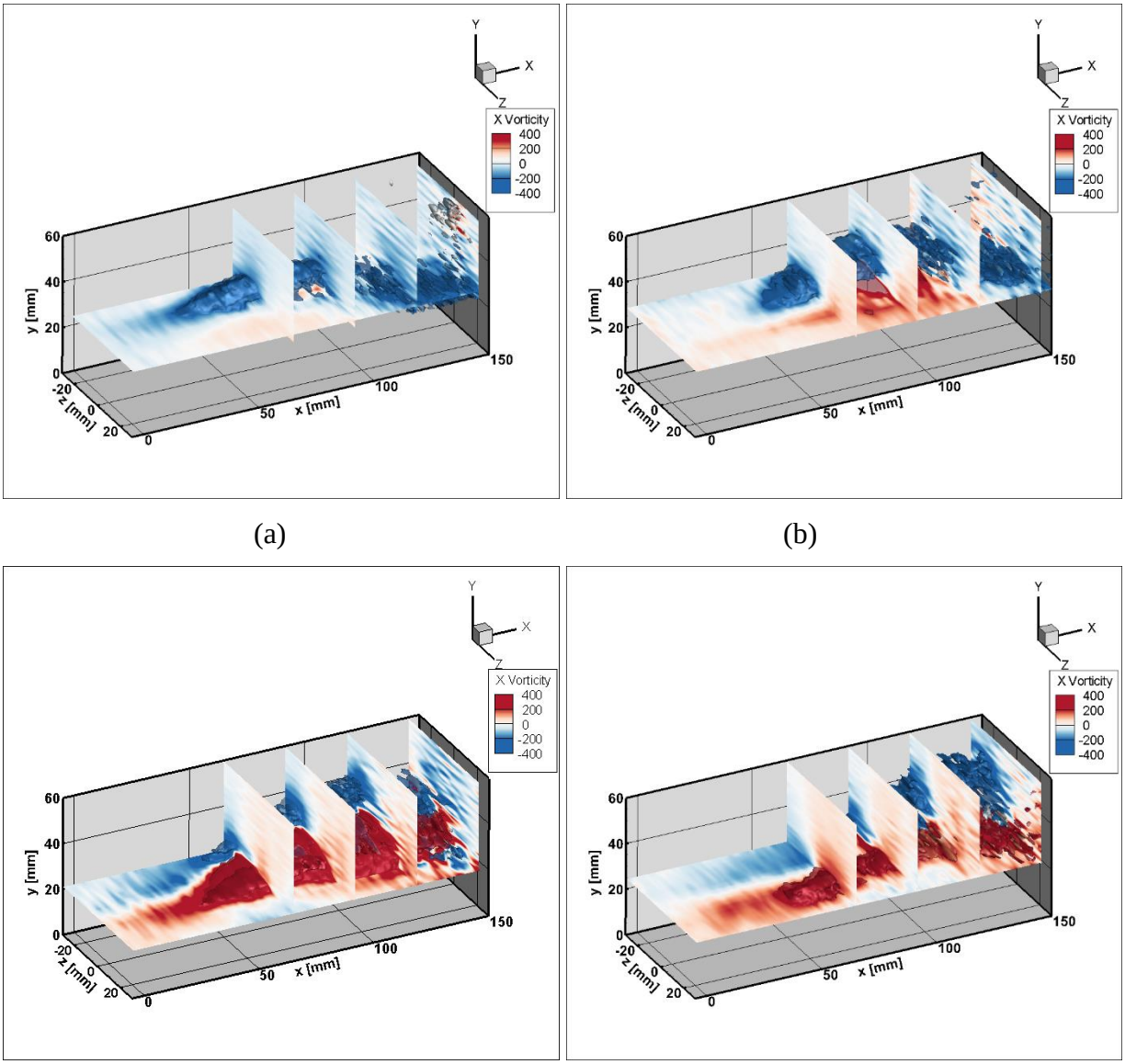

(a) (b)

(c) (d)

Fig. 3.18 Q-criterion isosurfaces colored by streamwise vorticity, ω_x, across a half oscillation for BR = 5 and (a) $\phi = 23.4°$, (b) $\phi = 68.4°$, (c) $\phi = 113.4°$, (d) $\phi = 158.4°$.

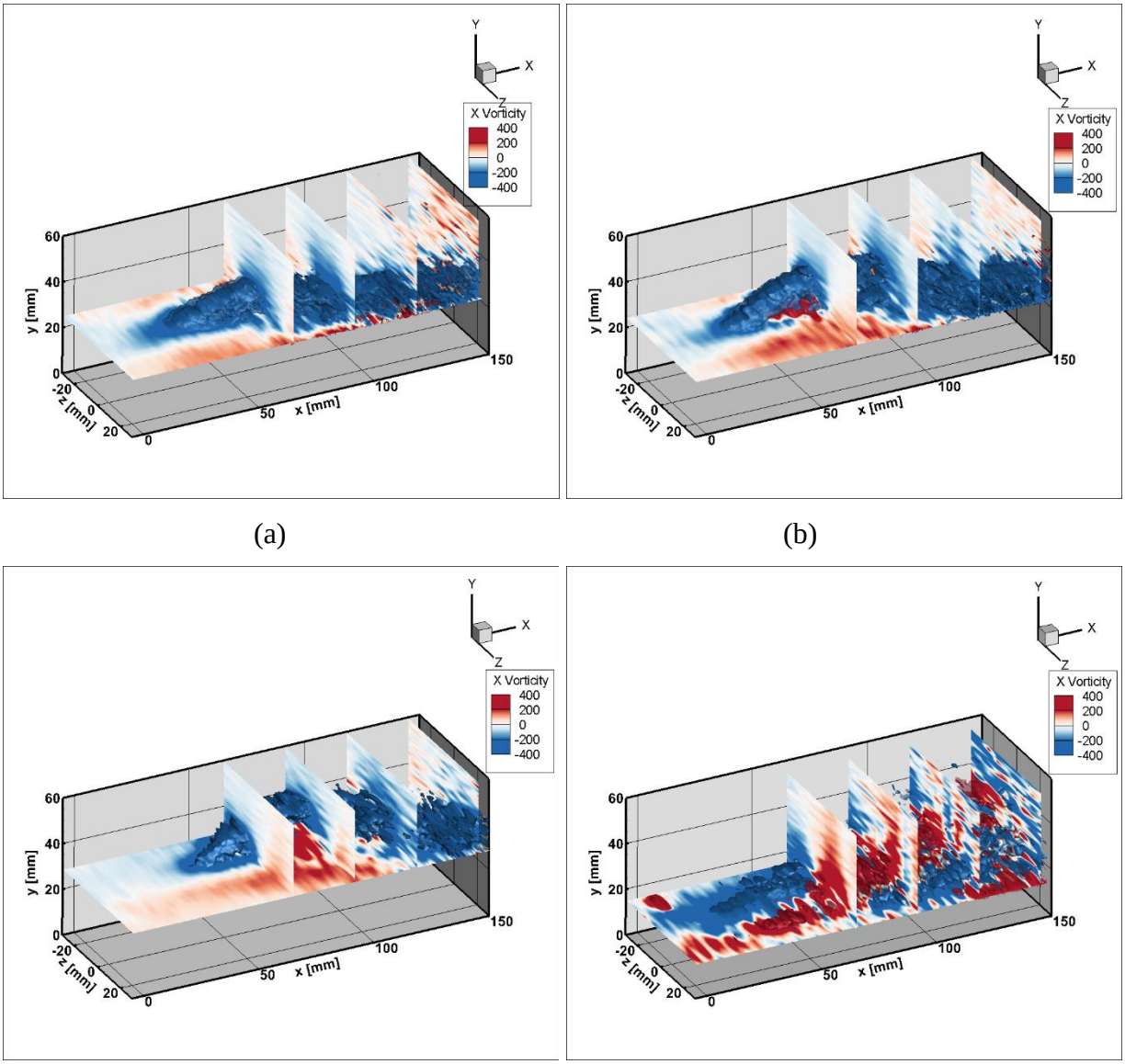

Fig. 3.19 Q-criterion isosurfaces colored by streamwise vorticity, ω_x, across a half oscillation for BR = 7 and (a) $\phi = 73.8°$, (b) $\phi = 118.8°$, (c) $\phi = 163.8°$, (d) $\phi = 208.8°$.

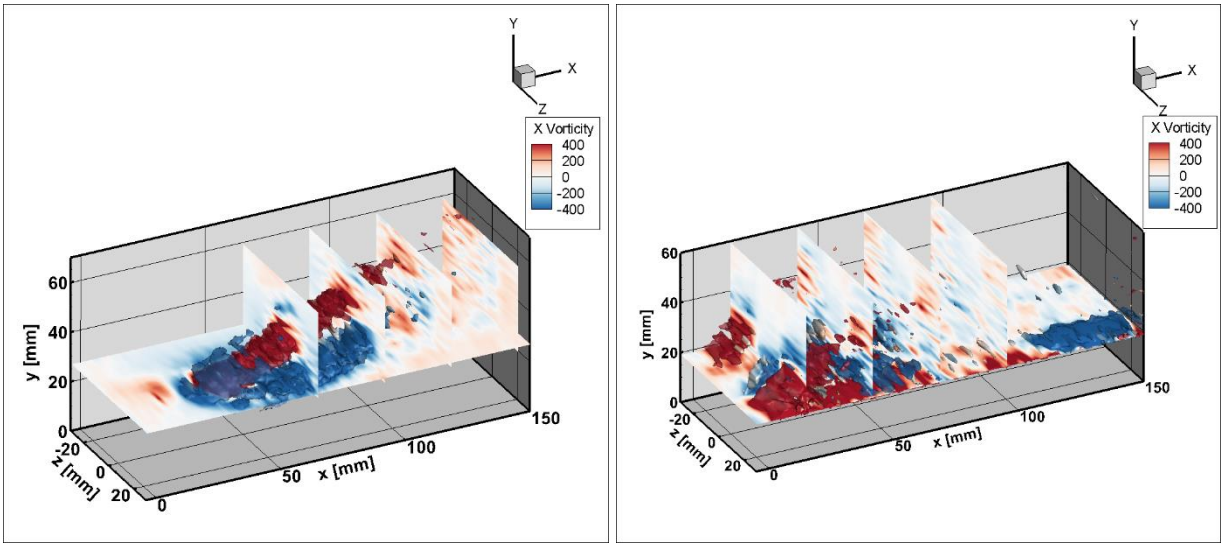

(a) (b)

Fig. 3.20 Q-criterion isosurfaces colored by streamwise vorticity, ω_x, across oscillator exit for BR = 3, ϕ = 64.8° and (a) α = 60°, (b) α = 90°.

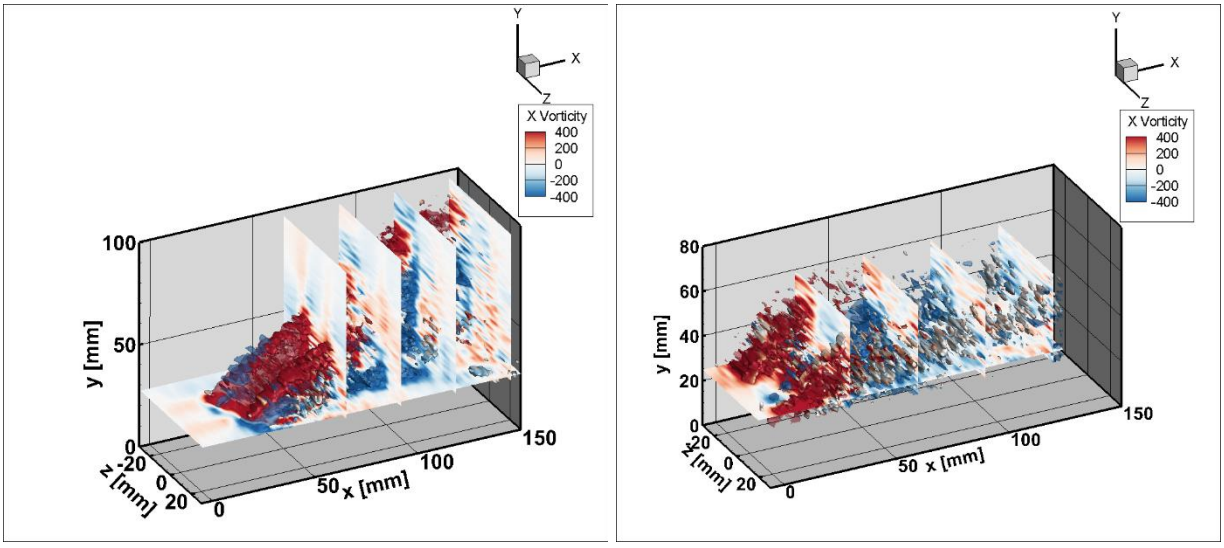

(a) (b)

Fig. 3.21 Q-criterion isosurfaces colored by streamwise vorticity, ω_x, across oscillator exit for BR = 5, ϕ = 68.4 and (a) α = 60°, (b) α = 90°.

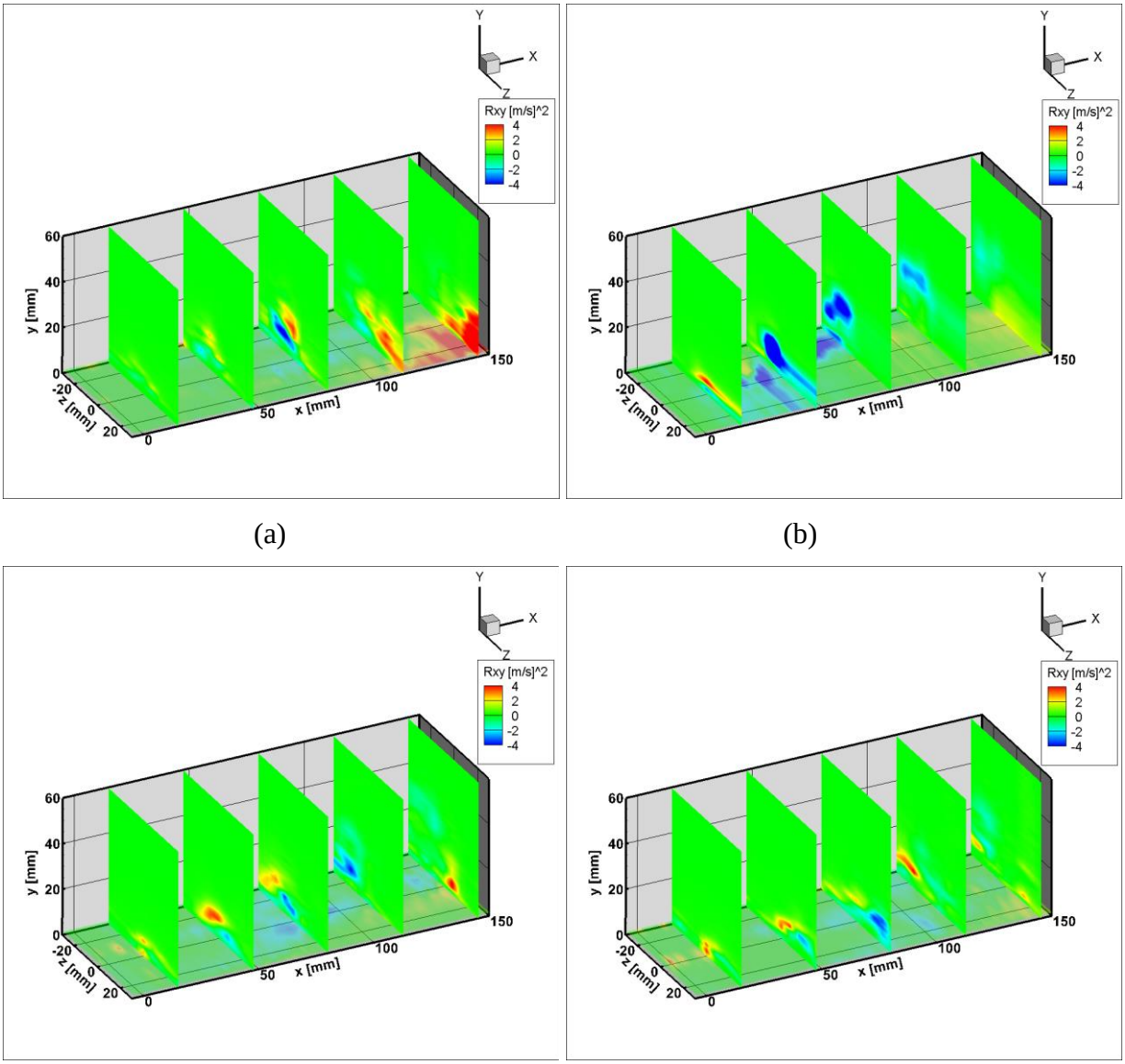

(a) (b)

(c) (d)

Fig. 3.22 Reynolds shear stresses, R_{xy}, for BR = 3 and (a) ϕ = 19.8°, (b) ϕ = 64.8°, (c) ϕ = 109.8°, (d) ϕ = 145.8°.

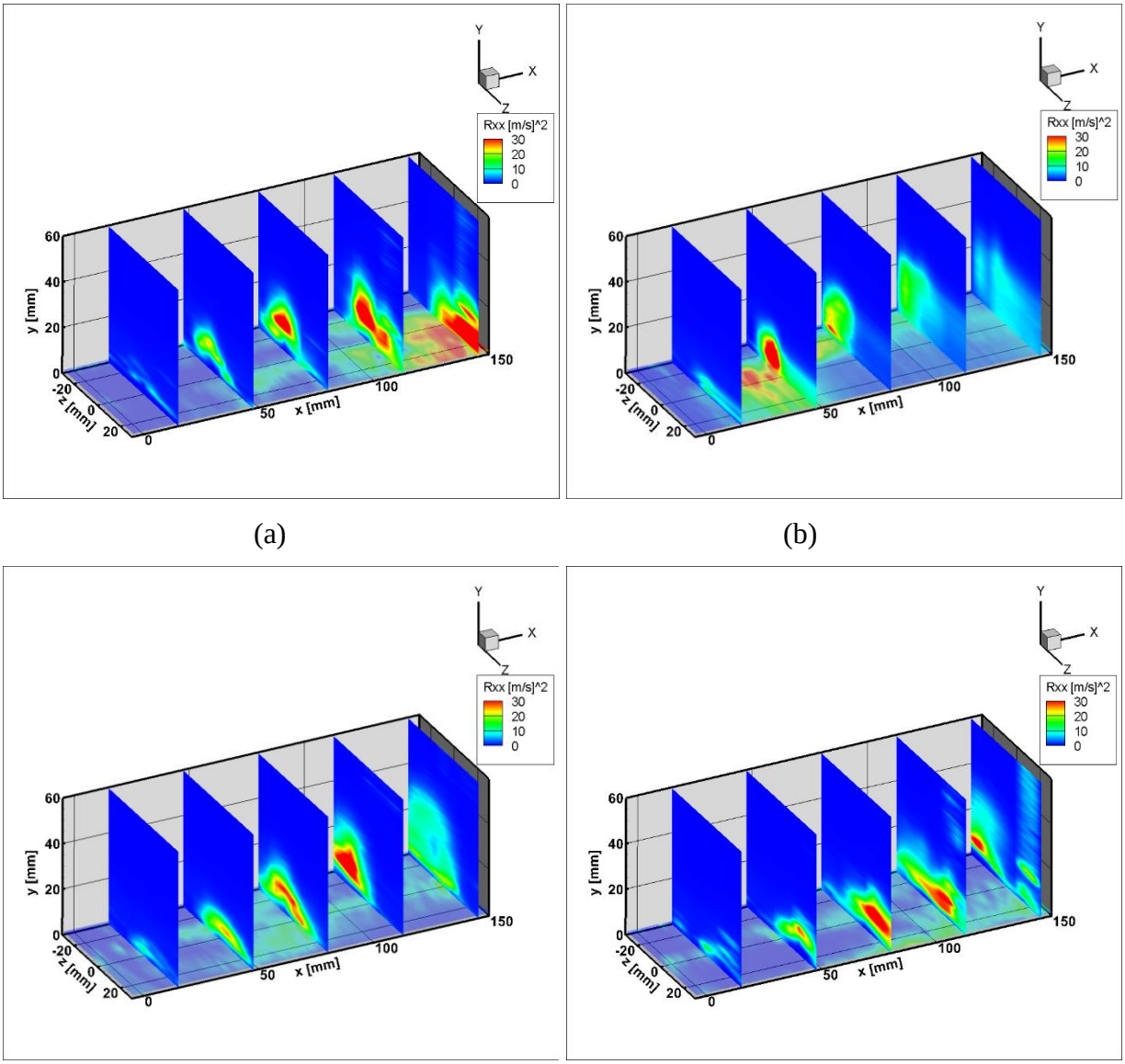

(a) (b)

(c) (d)

Fig. 3.23 Reynolds normal stresses, R_{xx}, for BR = 3 and (a) ϕ = 19.8°, (b) ϕ = 64.8°, (c) ϕ = 109.8°, (d) ϕ = 154.8°.

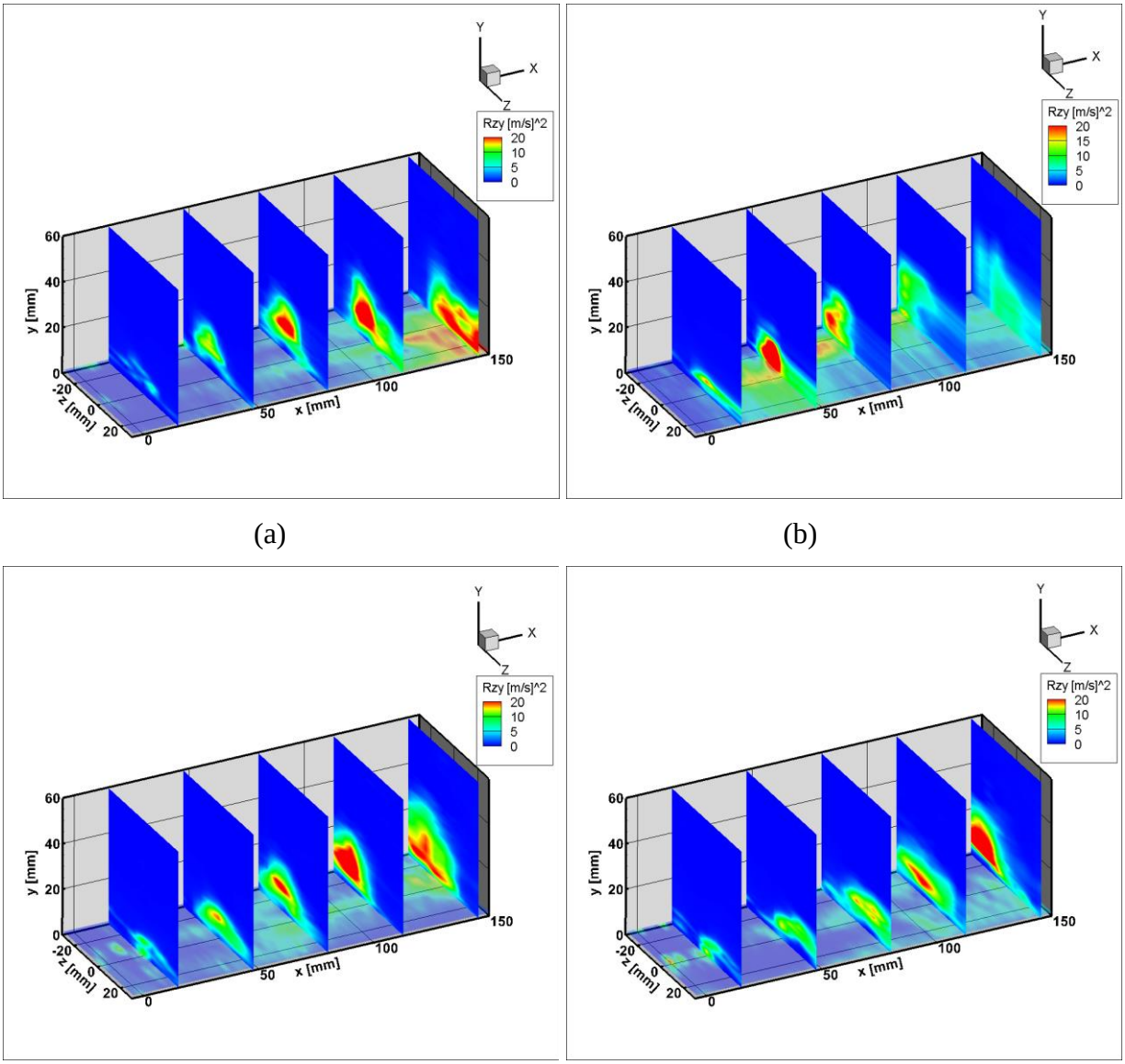

(a) (b)

(c) (d)

Fig. 3.24 Reynolds shear stresses, R_{zy}, for BR = 3 and (a) ϕ = 19.8°, (b) ϕ = 64.8°, (c) ϕ = 109.8°, (d) ϕ = 145.8°.

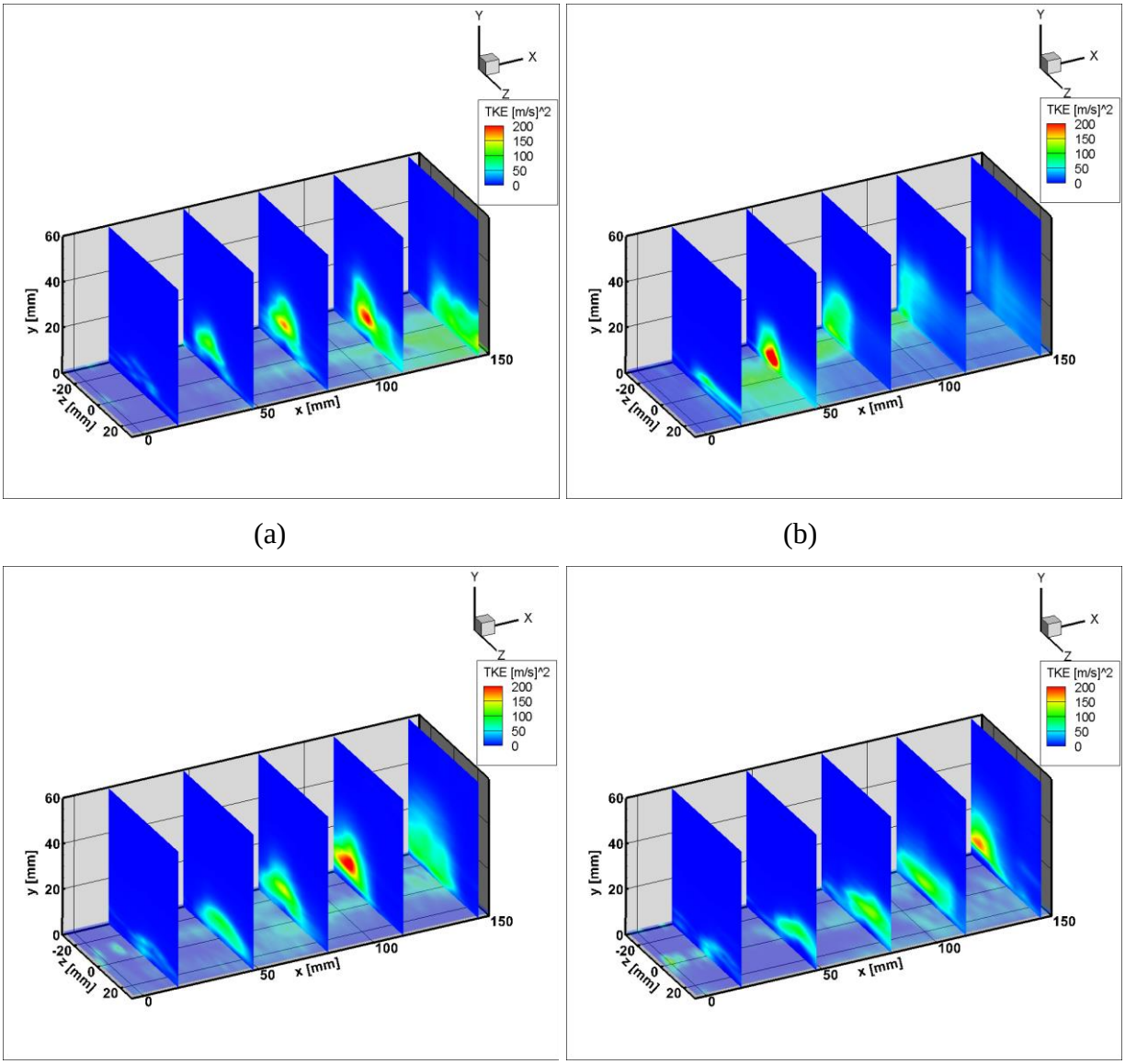

(a) (b)

(c) (d)

Fig. 3.25 Turbulent kinetic energy, TKE, for BR = 3 and (a) ϕ = 19.8°, (b) ϕ = 64.8°, (c) ϕ = 109.8°, (d) ϕ = 145.8°.

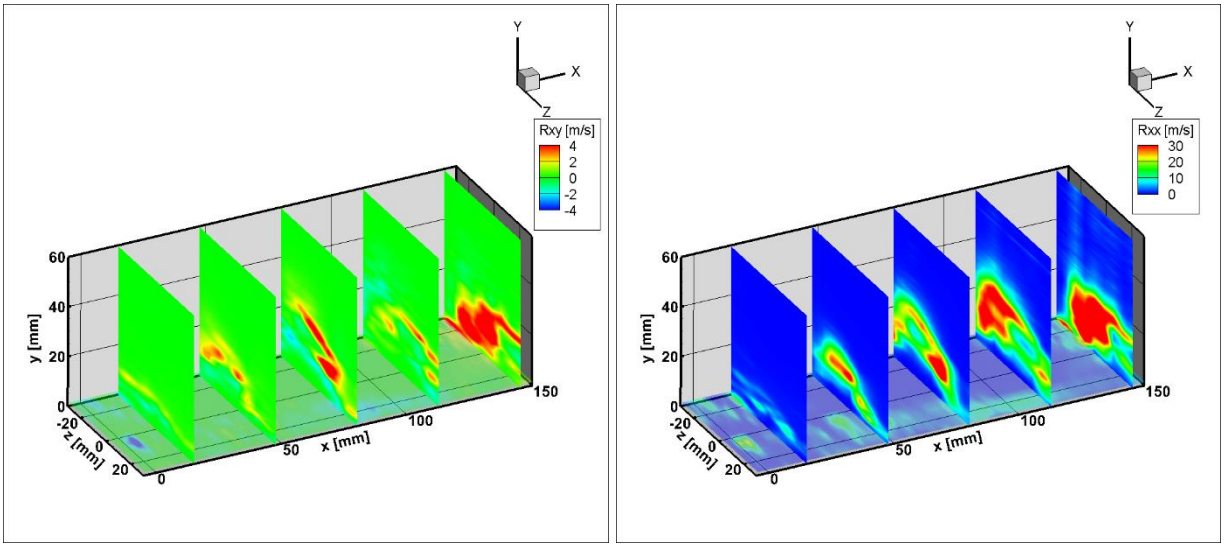

(a)

(b)

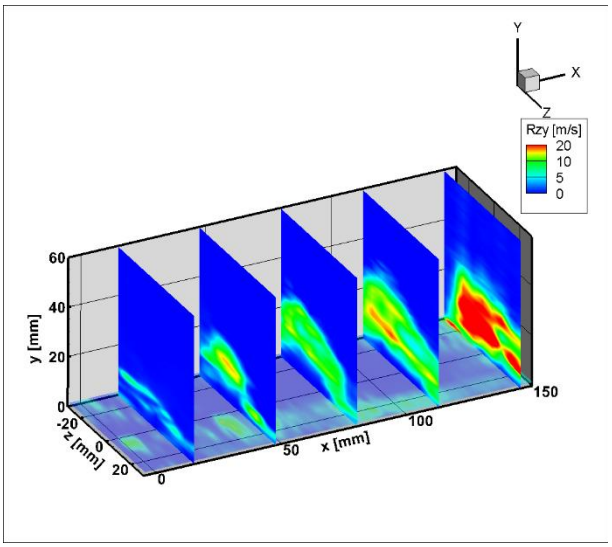

(c)

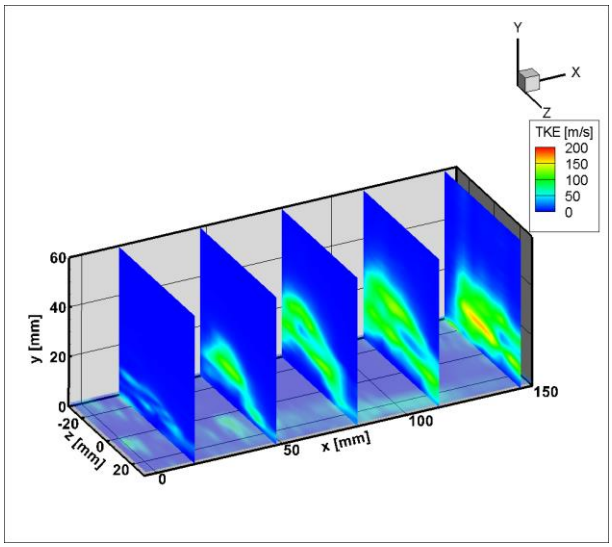

(d)

Fig. 3.26 Reynolds stresses (a) R_{xy}, (b) R_{xx}, (c) R_{zy} and turbulent kinetic energy, (d) TKE, for BR = 5 and ϕ = 68.4°.

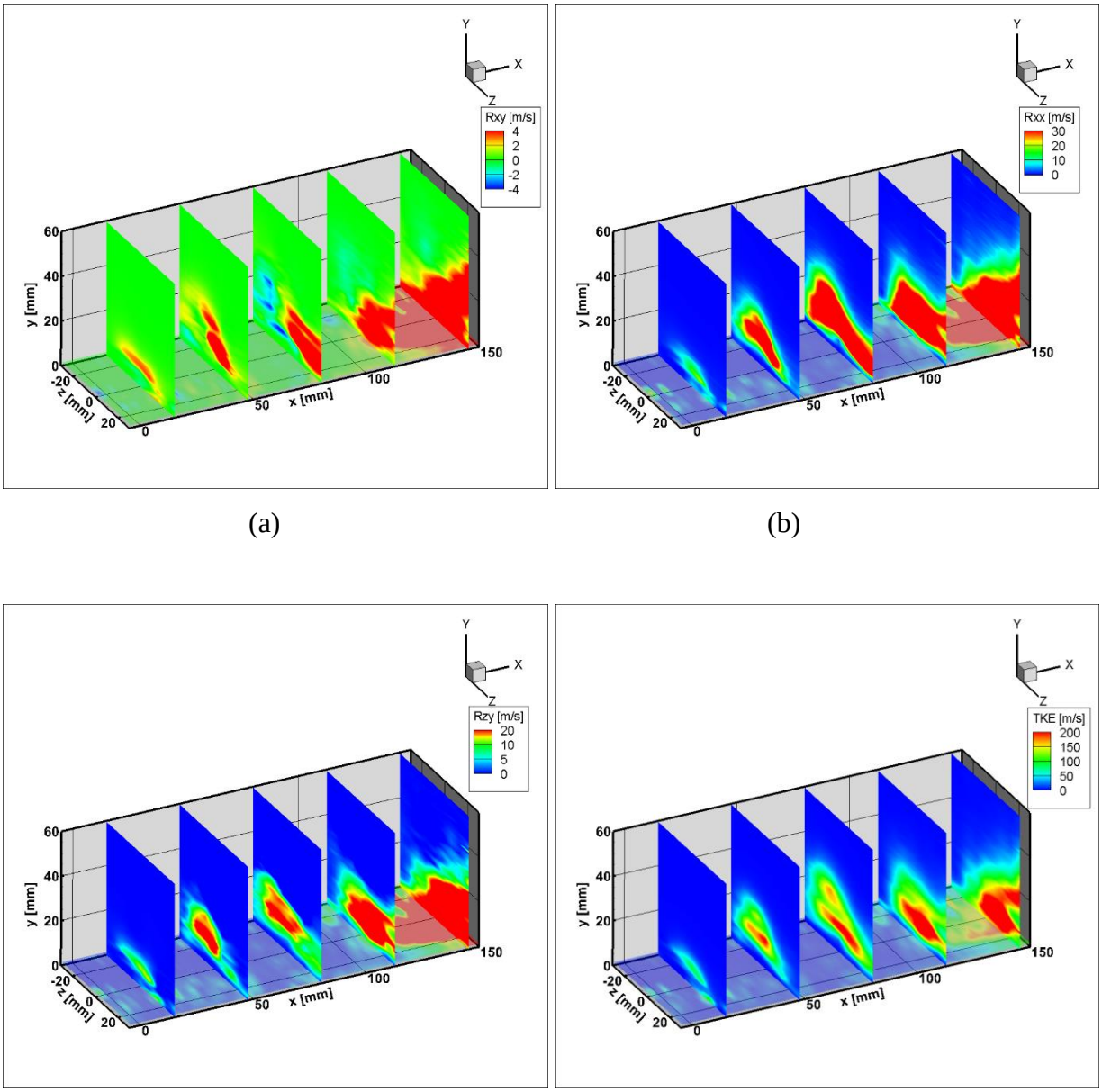

(a) (b)

(c) (d)

Fig. 3.27 Reynolds stresses (a) R_{xy}, (b) R_{xx}, (c) R_{zy} and turbulent kinetic energy, (d) TKE, for BR = 7 and $\phi = 118.8°$.

Chapter 4 Summary and Conclusions

An experimental study was performed to investigate the effect of blowing ratios and inclination angles on the flow interaction between an inclined oscillating jet and a crossflow. The jet's spatial oscillations were self-sustained and created through the presence of feedback channels within the fluidic oscillator geometry. Three-component stereoscopic PIV was performed using nine streamwise acquisition planes across the oscillator outlet. 700 image pairs were processed at each plane to obtain the three-dimensional flow field of the oscillator configurations of interest. For BR = 3 and BR = 5, three jet inclination angles, $\alpha = 30°$, $\alpha = 60°$ and $\alpha = 90°$, were investigated while for the fixed inclination of $\alpha = 30°$, three blowing ratios, BR = 3, BR = 5 and BR = 7, were considered. Phase-averaged flow fields were used to investigate the extent of the jet penetration in the wall-normal direction and to quantify the interactions produced with the incident boundary layer. Lateral spreading and dominant flow structures were investigated through isosurfaces of velocity and isosurfaces of Q-criterion colored by streamwise vorticity. Turbulence statistics showed the effect of changing blowing ratio on the mixing characteristics of the flow.

The sPIV velocity fields revealed higher wall-normal penetration of the jet into the crossflow as the blowing ratio increased. The curvature of the streamlines was also more pronounced as the blowing ratio increased due to the higher momentum injected into the flow. For $\alpha = 30°$ and BR = 3, the low momentum regions remained close to the wall and no interaction was observed between the low and high momentum regions. At BR = 5, lower momentum regions were entrained by the higher-momentum jet region, leading to more mixing. For the higher BR = 7, low momentum regions were hardly present due to the high momentum injected. As the blowing ratios increased, the influence of the jet reached a larger spanwise region, with high-momentum regions engulfing low momentum regions for BR = 5. However, both lateral and wall-normal penetration distances depended on the phase angle of the jet during the oscillation cycle. For phase angles corresponding to a case where the oscillating jet was directly aligned with the centerline, a higher

momentum transport was observed further downstream, at all blowing ratios. Due to the extent of the sPIV domain, lateral spreading of the jet at the phase angles for which the jet aligned with the extremities of the oscillator outlet could not be fully quantified.

For the fixed BR = 3 and BR = 5 cases, the wall-normal penetration height increased at higher inclination angles. However, the wall normal penetration for $\alpha = 90°$ decayed in the far field due the normal orientation of the jet with respect to the crossflow. The high-momentum regions were pushed further away from the wall for $\alpha = 60°$ and $\alpha = 90°$, as compared to $\alpha = 30°$. For $\alpha = 60°$, momentum injection into the boundary layer was limited to near field of the oscillator outlet while most of the flow field above the outlet was affected for $\alpha = 90°$. Furthermore, two high-momentum lobes emerged on either side of the oscillator center plane at $\alpha = 90°$again due to the normal orientation of the jet with respect to the crossflow.

For BR = 3, isosurfaces of Q-criterion colored by streamwise vorticity showed the presence of dominant counter-rotating vortices at two phase angles located 180° out of phase of each other across a full oscillation cycle. A slight variation in the streamwise flow field was identified between those two phase angles due to the jet's asymmetry with respect to the oscillator centerline. Between those two phase angles, the jet produced weaker residual vortex structures. This alternating vortex pair is analogous to the one observed at low blowing ratios in previous studies with $\alpha = 90°$. For the higher blowing ratios, the secondary residual vortices with opposite vorticity were larger but had overall lower vortical intensity. The larger and weaker vortex cores, which also deflected farther in the lateral direction, promoted higher spanwise mixing at BR = 5 and BR = 7. Vortex formation for $\alpha = 60°$ revealed that secondary vortices became "stacked" above primary vortices as they propagated downstream across the oscillation. Vortex pairs with opposite vorticity compared to the main structures for $\alpha = 30°$ and $\alpha = 60°$ were observed at $\alpha = 90°$. The normal orientation of the jet with respect to the crossflow introduces a spanwise component vorticity from the outlet leading edge vortices, reducing the overall streamwise vorticity strength at $\alpha = 90°$.

The Reynolds shear stresses, R_{xy}, were the driving mechanisms behind the formation of the vortices across the oscillation cycle, with positive and negative regions of R_{xy} which coincides with vortical regions for BR = 3. For both BR = 5 and BR = 7, a lag between the R_{xy} shear location and the location of the vortex pairs was noticed, leading to the larger and weaker vortices generated

at those blowing ratios. The contribution of u' to the streamwise momentum was captured through normal shear stress R_{xx}. The R_{xx} components were similar to the velocity isosurfaces for all blowing ratios and contributed the most to the downstream convection of the jet. The R_{zy} shear stresses contributed to the lateral jet deflection and the wall-normal penetration mainly in the near field of the oscillator outlet and increased with blowing ratio. The turbulent kinetic energy showed the contribution of all the turbulent fluctuations and increased with higher blowing ratios. The propagation of the maximum TKE location across the oscillation cycle indicated that the turbulent iteration with the crossflow were most significant when the jet was primarily aligned with the crossflow then propagated through the flow field as the phase angle changed over time.

These observations are consistent with earlier studies that considered the extent of jet penetration and lateral spreading due to the influence of changing blowing ratios on a 90° oscillating jet into a crossflow. The additional information provided in this investigation for α = 30° and α = 60° suggest that a good starting point for active flow would be a combination of BR = 5 and α = 60°. Such blowing ratio provided enough entrainment of momentum to favor mixing and vortex formation while an inclination of 60° allowed the jet to interact with the boundary layer in the near field of the oscillator outlet and to propagate further downstream and into the wall-normal direction. However, to consider the use of such fluidic oscillator for active flow control, the complete flow field for α = 60°and α = 90° need to be investigated to confirm these preliminary observations. For the current oscillator design, the mass flow rate is related to the oscillator frequency and thus the blowing ratio is coupled with the jet frequency. Consequently, the results of this study can be scaled to oscillators with the same internal geometry and working fluid if compressibility effects remain negligible.

Chapter 5 Uncertainty Analysis

The uncertainty associated with the experimental observations and results are presented in this chapter. Taking into account such uncertainties is important to evaluate the extent of the scatter associated with the experimental results over multiple trials and to provide a reasonably complete picture of the reliability of the experiment. Kline and McClintock defined the uncertainty in a measurement as the "possible value that an error may have". Two sources of errors provide the best estimate of measurement error and mainly contribute to the overall uncertainties in this study. The first one, known as "bias" error, include personal, instrumental and method errors, which stem from the measurement capabilities of given equipment, the accuracy of calibration or the degree of control over the experiment. These errors are also considered "fixed" since they alter the true value in one way only during a complete experiment. The second source of uncertainty is "precision" error. This error behaves randomly with a zero mean[24] and contributes to different offsets from the mean value over time.

Both the "bias" and "precision" errors are assumed to represent stationary statistical properties of a normally distributed data set and thus error observations are independent of one another. The "precision" uncertainty, U_X, associated with N samples of the variable X with mean $\overline{X_n}$ is given by

$$U_{\bar{X}} = \frac{t^* S_X}{\sqrt{N}} \tag{5.1}$$

where is the student's t^* statistic for the desired confidence level and appropriate degree of freedom, S_X is the standard deviation of the sample of size N used to compute the mean value $\overline{X_n}$[24]. For a given experiment a result value, R, is computed from several independent variables, x_i, and can be expressed as a function of such variables according to

$$R = R(x_1, x_2, \dots, x_n) \tag{5.2}$$

The "bias" uncertainty, U_R, associated with the result, R, is expressed at the same confidence levels as were used to obtain the uncertainties of each x_i independent variable by taking a root-square-sum of the uncertainties of each variable that contribute to the result[23]. The "bias" uncertainty can be obtained using

$$U_R = \sqrt{\left(\frac{\partial R}{\partial x_1} U_{x_1}\right)^2 + \left(\frac{\partial R}{\partial x_2} U_{x_2}\right)^2 + \cdots + \left(\frac{\partial R}{\partial x_n} U_{x_n}\right)^2} \tag{5.3}$$

The methods described above were the basis for calculations of 'bias" uncertainties associated with the flow conditions and oscillator jet conditions and "precision" uncertainty associated with the sPIV measurements. These are presented in detail in sections 5.1 and 5.2.

5.1 Uncertainty in Flow Field Conditions

5.1.1 Uncertainty in Crossflow conditions

The uncertainties associated with the crossflow conditions were calculated using the equations in this section. Estimates of uncertainty in observed variables such as the freestream dynamic pressure, atmospheric density, dynamic viscosity and freestream velocity are presented in Table 5.1.

The uncertainty associated with the dynamic pressure depended only on the pressure difference between the settling and test sections. This was due to the negligible uncertainty in the constant area ratio variable in. Eq. 2.3. This dynamic pressure uncertainty was calculated, according to,

$$U_{q_\infty} = \sqrt{\left(\frac{\partial q_\infty}{\partial (P_{ss} - P_{ts})} U_{(P_{ss} - P_{ts})}\right)^2} \tag{5.4}$$

where, $U_{(P_{ss} - P_{ts})}$, the uncertainty in the uncertainty in the measured pressure difference between the settling section and the test section, was assumed constant and simplified Eq. 5.4 to

$$U_{q_\infty} = \frac{\partial q_\infty}{\partial (P_{ss} - P_{ts})} U_{(P_{ss} - P_{ts})} = \frac{1}{1 - \left(\frac{A_{ts}}{A_{ss}}\right)^2} U_{(P_{ss} - P_{ts})} \tag{5.5}$$

The only factors that contributed to the uncertainty of ρ_{amb} were P_{amb} and T_{amb}, since the parameter R in the ideal gas equation is a constant for the air. The calculated uncertainty was obtained using

$$U_{\rho_{amb}} = \sqrt{\left(\frac{\partial \rho_{amb}}{\partial P_{amb}} U_{P_{amb}}\right)^2 + \left(\frac{\partial \rho_{amb}}{\partial T_{amb}} U_{T_{amb}}\right)^2} \tag{5.6}$$

where

$$\frac{\partial \rho_{amb}}{\partial P_{amb}} = \frac{1}{RT_{amb}} \tag{5.7}$$

$$\frac{\partial \rho_{amb}}{\partial T_{amb}} = -\frac{P_{amb}}{RT_{amb}^2} \tag{5.8}$$

The test section velocity can also be formulated as a function of the dynamic pressure and ambient density according to,

$$U_\infty = U_{ts} = \sqrt{\frac{2q_\infty}{\rho_{amb}}} \tag{5.9}$$

Using the previously obtained uncertainties U_{q_∞} and $U_{\rho_{amb}}$, the uncertainty in the freestream velocity was calculated as follows,

$$U_{U_\infty} = \sqrt{\left(\frac{\partial U_\infty}{\partial q_\infty} U_{q_\infty}\right)^2 + \left(\frac{\partial U_\infty}{\partial \rho_{amb}} U_{\rho_{amb}}\right)^2} \tag{5.10}$$

where

$$\frac{\partial U_\infty}{\partial q_\infty} = \frac{1}{\sqrt{2q_\infty \rho_{amb}}} \tag{5.11}$$

$$\frac{\partial U_\infty}{\partial \rho_{amb}} = -\frac{1}{\rho_{amb}} \sqrt{\frac{q_\infty}{2\rho_{amb}}} \tag{5.12}$$

5.1.2 Uncertainty in Jet Conditions

Using the expression for BR and Eq. 2.6, the jet velocity was calculated as follows,

$$U_{jet} = \frac{\dot{m}}{\rho_{amb} l_o t} \tag{5.13}$$

The uncertainties associated with the jet velocity and blowing ratio were calculated using the following equations.

$$U_{U_{jet}} = \sqrt{\left(\frac{\partial U_{jet}}{\partial \dot{m}} U_{\dot{m}}\right)^2 + \left(\frac{\partial U_{jet}}{\partial \rho_{amb}} U_{\rho_{amb}}\right)^2 + \left(\frac{\partial U_{jet}}{\partial l_0} U_{l_o}\right)^2 + \left(\frac{\partial U_{jet}}{\partial t} U_t\right)^2} \tag{5.14}$$

$$U_{BR} = \sqrt{\left(\frac{\partial BR}{\partial U_{jet}} U_{U_{jet}}\right)^2 + \left(\frac{\partial BR}{\partial U_\infty} U_{U_\infty}\right)^2} \tag{5.15}$$

where

$$\frac{\partial U_{jet}}{\partial \dot{m}} = \frac{1}{\rho_{amb} l_o t} \tag{5.16}$$

$$\frac{\partial U_{jet}}{\partial \rho_{amb}} = -\frac{\dot{m}}{\rho_{amb}^2 l_o t} \tag{5.17}$$

$$\frac{\partial U_{jet}}{\partial l_o} = -\frac{\dot{m}}{\rho_{amb} l_o^2 t} \tag{5.18}$$

$$\frac{\partial U_{jet}}{\partial l_t} = -\frac{\dot{m}}{\rho_{amb} l_o t^2} \tag{5.19}$$

$$\frac{\partial BR}{\partial U_{jet}} = \frac{1}{U_\infty} \tag{5.20}$$

$$\frac{\partial BR}{\partial U_\infty} = -\frac{U_{jet}}{U_\infty^2} \tag{5.21}$$

Table 5.2 shows examples of these calculated variables and their corresponding uncertainties.

5.2 PIV Uncertainty Analysis

Using the methods described by Lazar et al.[25], the resulting "sampling" uncertainties associated with the PIV measurements were also calculated. All those uncertainties have error sources that are directly embedded into the characteristics of the recorded images. However, some of those uncertainties, especially those due to bias errors, are hidden and cannot be quantified through an analysis of the PIV images[26]. Therefore, four main sources of uncertainties are

accounted for to capture the 'hidden' errors: equipment uncertainty, uncertainty in particle dynamics, sampling, and processing uncertainties[25].

Equipment uncertainty (U_E) accounted for uncertainties due to the timing and the accuracy of the sPIV synchronization and trigger system, image distortion and calibration scale. For this experiment, perspective errors were low due to the use of the second sCMOS camera and the Scheimplflug adapter, while errors associated with image noise were reduced by applying a background subtraction. Calibration errors were small due to the self-calibration feature in the LaVision DaVis software package and the use of the 3D calibration plate[27]. Uncertainties associated with those bias errors were considered to be negligible.

The particle dynamics uncertainty, U_D, included both the out-of-plane motion of the seed particles and the lag in particle motion relative to the surrounding fluid as dictated by Stokes' drag law. This particle slip velocity, u_s, can be estimated as the difference between the velocity of the seed particle, u_p, and the surrounding fluid velocity, u_f,[28]

$$u_s = u_p - u_f = \frac{1}{18}\frac{(\rho_p - \rho_f)d_p^2}{\mu_f}\left(\frac{\partial u_p}{\partial x_p}\frac{\partial x_p}{\partial t} + \frac{\partial u_p}{\partial y_p}\frac{\partial y_p}{\partial t}\right) \tag{5.22}$$

where ρ_p is the density of the seed particles, ρ_f is the fluid density, d_p is the particle diameter, μ_f is the fluid viscosity, and x_p and y_p represent the local coordinate directions.

The phased-averaged velocity fields and the derived statistics in this study were obtained from statistically independent and normally distributed instantaneous images. The scatter associated with the vector fields in those instantaneous images was accounted for through the sampling uncertainty, U_s. The "precision" sampling uncertainty was evaluated as outlined in the beginning of this chapter, using a confidence level of 95% and the following equation,

$$\sigma_V = \overline{\boldsymbol{X_n}} \pm \frac{t^* S_X}{\sqrt{N}} \tag{5.23}$$

with σ_V representing the scatter in the mean flow velocity and the previously defined parameters $\overline{X_n}$, t^*, S_X and N.

The processing uncertainty, U_p, was used to assess the accuracy and reliability of the digital processing techniques used to obtain instantaneous vector fields from the raw particle image pairs. This processing uncertainty mainly takes into account the cross-correlation methods while also capturing error sources embedded in recorded PIV images. The uncertainty quantification method

in the LaVision DaVis software package is based on Wieneke's correlation statistics approach[29]. The technique considers how individual pixels contribute to the cross-correlation peak to obtain the displacement vector uncertainty. Then, an uncertainty value is generated for individual instantaneous velocity vector fields. Appropriate uncertainty propagation techniques[30] are finally used to independently compute uncertainties for the u, v and w velocity components and the derived flow statistics.

The total PIV uncertainty, U_T, included the overall sPIV measurement error and was calculated as the root of the sum of the squares of the individual uncertainties from the four main sources of sPIV errors. The total uncertainty was given by,

$$U_T = \sqrt{{U_E}^2 + {U_D}^2 + {U_s}^2 + {U_P}^2} \tag{5.24}$$

The uncertainties associated with PIV acquisition for the flow field of a 30° inclined oscillator ejecting into the crossflow for BR = 3 and ϕ = 64.8° were calculated and the sample results were shown in Fig. 5.1 through Fig. 5.4 .These figures present the uncertainties in the streamwise, transverse and spanwise directions normalized by the average velocity components across the flow field velocity. The mean uncertainties of the velocity fields in the x-, y- and z-directions were calculated to be 0.16%, 0.13% and 0.46% respectively.

5.3 Chapter 5 Tables

Table 5.1 Example of uncertainties for flow conditions of α = 30° oscillator at BR = 3 and ϕ = 19.8°

Parameter	Reference Value	Absolute Uncertainty	% Relative Uncertainty
q_∞	91.507 Pa	±5.124 Pa	±5.5996
P_{amb}	99229.347 Pa	±55.158 Pa	±0.0556
T_{amb}	294.106 K	±1 K	±0.3400
ρ_{amb}	1.1756 kg/m^3	±0.00405 kg/m^3	±0.3445
U_∞	12.472 m/s	±0.35001 m/s	±2.8063

Table 5.2 Example of uncertainties for oscillator jet conditions at α = 30°oscillator, BR = 3 and ϕ = 19.8°

Parameter	Reference Value	Absolute Uncertainty	% Relative Uncertainty
$\dot{m}$	188 SLPM	±3.504 SLPM	±1.8638
U_{jet}	39.194 m/s	±0.7418 m/s	±1.8926
BR	3.143	±0.1064	±3.3853

5.4 Chapter 5 Figures

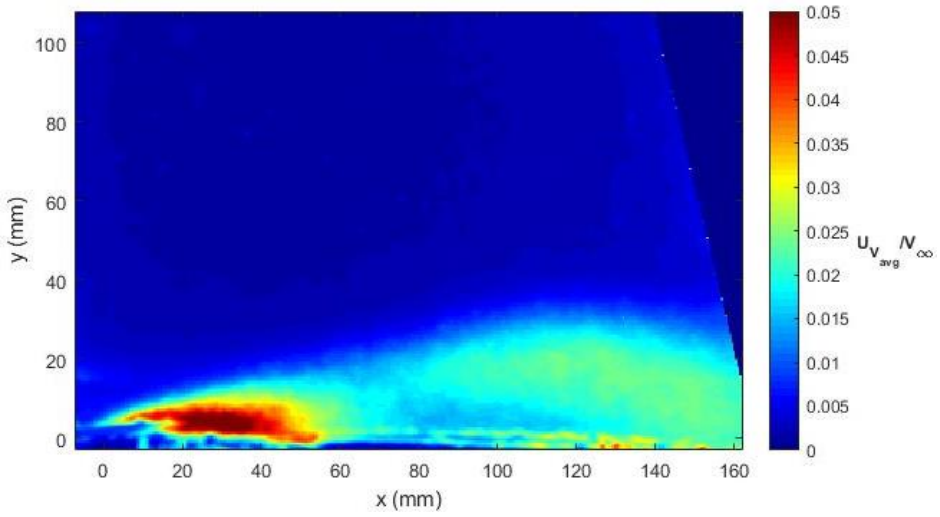

Fig. 5.1 Normalized uncertainties in the average velocity at the center plane for BR = 3 and ϕ = 64.8° .

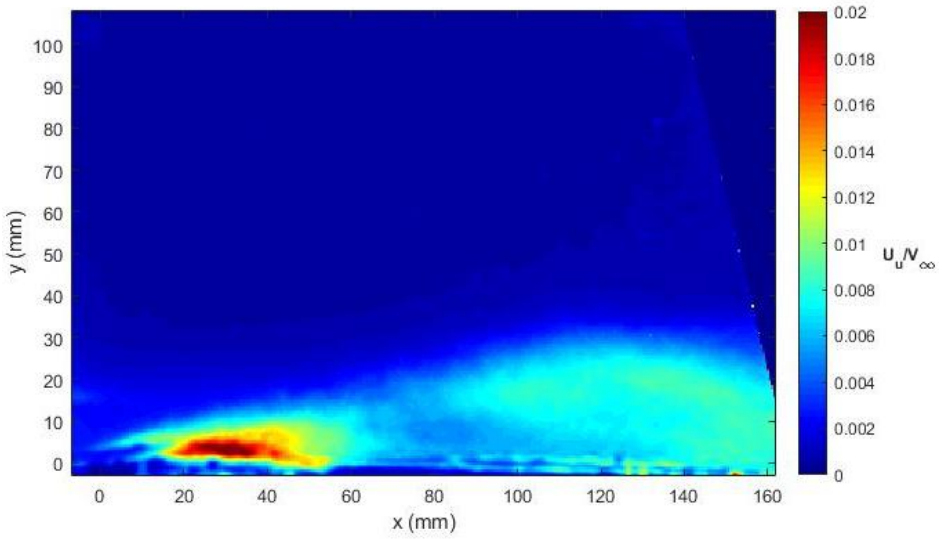

Fig. 5.2 Normalized streamwise uncertainties at the center plane for BR = 3 and ϕ = 64.8° .

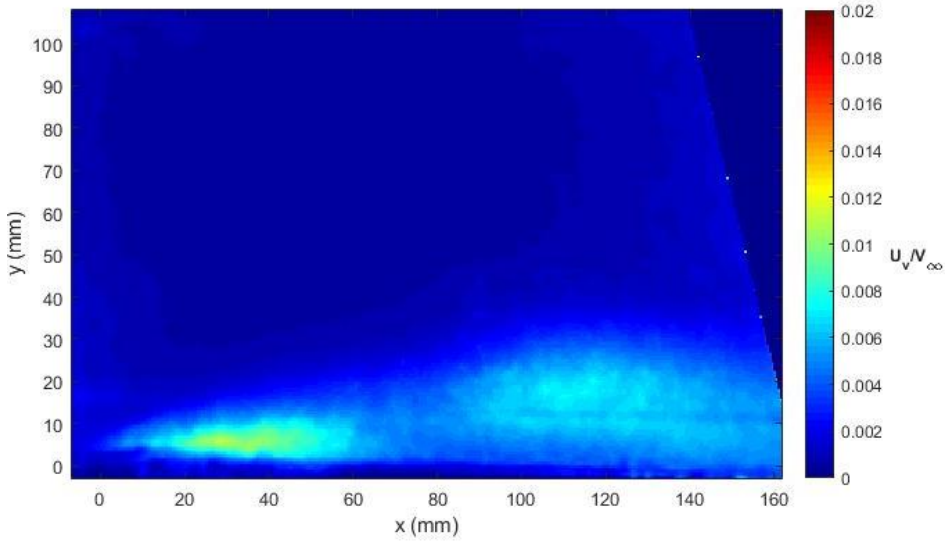

Fig. 5.3 Normalized transverse uncertainties at the center plane for BR = 3 and ϕ = 64.8° .

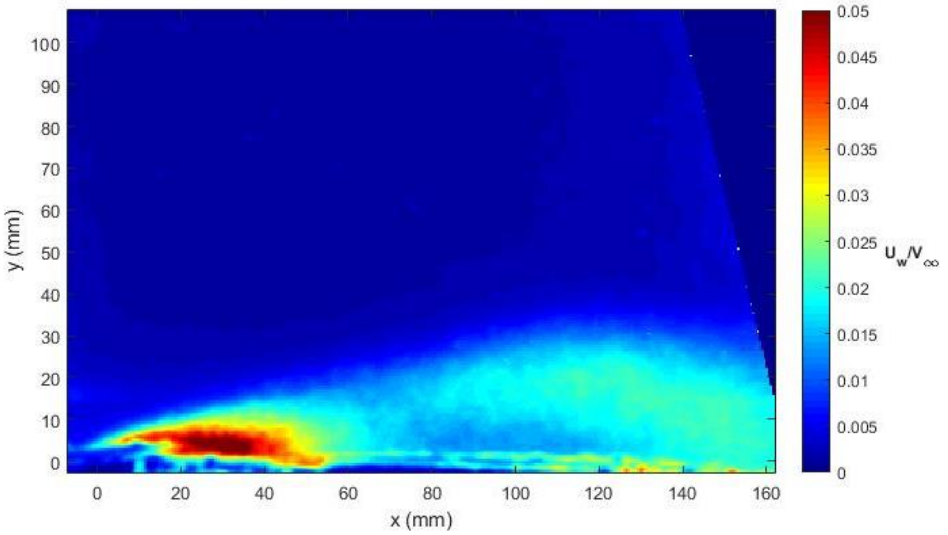

Fig. 5.4 Normalized spanwise uncertainties at the center plane for BR = 3 and ϕ = 64.8° .

References

[1] Stouffer, R., and Bower, R., 'Fluidic Flow Meter with Fiber Optic Sensor", US Patent 5827976, 1998.

[2] Gaertlein, S., Woszidlo, R., Ostermann, F., Nayeri, C., and Paschereit, C. O., "The Time-Resolved Internal and External Flow Field Properties of a Fluidic Oscillator," 52nd AIAA Aerospace Sciences Meeting, Jan 2014.

[3] Woszidlo R., Ostermann, F., Schmidt, H., "Fundamental Properties of Fluidic Oscillators for Flow Control Applications," *AIAA Journal,* Volume 57, Number 3, March 2019.

[4] Ostermann, F., Woszidlo, R., Nayeri, C., and Paschereit, C. O., "Properties of a sweeping jet emitted from a fluidic oscillator" *Journal of Fluid Mechanics* (2018), Volume 857, pp. 216-238.

[5] Koklu, M., "The Effects of Sweeping Jet Actuator Parameters on Flow Separation Control,"45th AIAA Fluid Dynamics Conference, 22-26 June 2015, Dallas TX, AIAA Paper 2015-2485.

[6] DeSalvo, M., Whalen, E., Glezer, A., "High-Lift Enhancement Using Active Flow Control," 29th AIAA Applied Aerodynamics Conference, 27-30 June 2011, Honolulu HW, AIAA Paper 2011-3355.

[7] Hossain, M., Prenter, R., Lundgreen, R., Ameri, A., Gregory, J.W., Bons, J.P., "Experimental and Numerical Investigation of Sweeping Jet Film Cooling". *Journal of Turbomachinery*, 140(3):031009, Dec 2017. doi:10.1115/1.4038690.

[8] Guyot, D., Paschereit, C., Raghu, S., "Active Combustion Control Using a Fluidic Oscillator for Asymmetric Fuel Flow Modulation," *International Journal of Flow Control,* Volume 1, Number 2, 2009.

[9] Raman, G., Raghu, S., "Miniature Fluidic Oscillators for Flow and Noise Control," AIAA Fluids 2000 Conference and Exhibit, 19-22 June 2000, Denver CO, AIAA Paper A00-33886.

[10] Ostermann, F., Woszidlo R., Nayeri, C., Paschereit, C., "The Time-Resolved Flow Field of a Jet Emitted by a Fluidic Oscillator into a Crossflow," 54th AIAA Aerospace Sciences Meeting, 4-8 January 2016, San Diego CA, AIAA Paper 2016-0345.

[11] Ostermann, F., Woszidlo R., Nayeri, C., Paschereit, C., "The interaction between a spatially oscillating jet emitted by a fluidic oscillator and a cross-flow," *Journal of Fluid Mechanics* (2019),

Volume 863, pp. 215-241.
[12] Ostermann, F., Woszidlo R., Nayeri, C., Paschereit, C., "Effect of Velocity Ratio on the Flow Field of a Spatially Oscillating Jet in Crossflow," 55th AIAA Aerospace Sciences Meeting, 9-13 January 2017, Grapevine TX, AIAA Paper 2017-0769.
[13] Aram, S., Shan, H., "Computational Analysis of Interaction of a Sweeping Jet with an Attached Crossflow," *AIAA Journal*, Volume 57, Number 2, February 2019.
[14] Ostermann, F., Woszidlo R., Nayeri, C., Paschereit, C., "Interaction between a Jet emitted by a Fluidic Oscillator and a Crossflow at a Skew Angle," 57th AIAA Aerospace Sciences Meeting, 7-11 January 2019, San Diego CA, AIAA Paper 2019-0887.
[15] Hossain, M., Prenter, R., Lundgreen, R., Agricola, L., Ameri, A., Gregory, J., Bons, J., "Investigation of Crossflow Interaction of an Oscillating Jet," 55th AIAA Aerospace Sciences Meeting, 9-13 January 2017, Grapevine TX, AIAA Paper 2017-1690.
[16] Mehti Koklu, "The Effects of Sweeping Jet Actuator Parameters on Flow Separation Control", 45th AIAA Fluid Dynamics Conference, 22-26 June 2015, Dallas, TX, AIAA Paper 2015-2485.
[17] Colletti, C., Awate, V., Ansell, P., "Effect of Geometric Parameters and Flow Conditions on the Frequency of Fluidic Oscillators for Active Flow Control", 57th AIAA Aerospace Sciences Meeting, 7-11 January 2019, San Diego CA, AIAA Paper 2019-0292.
[18] Batchelor, G. K., "An introduction to fluid dynamics," Cambridge university press, 2000.
[19] Brenden Epps, "Review of Vortex Identification Methods", 55th AIAA Aerospace Sciences Meeting, 9–13 January 2017, AIAA Paper 2017-0989.
[20] Hunt, J. C. R., Wray, A., Moin, P., "Eddies, stream, and convergence zones in turbulent Flows", Center for Turbulence Research Report CTR-S88, 1988.
[21] Jeong, J., Hussain, F., "On the identification of a vortex", *Journal of Fluid Mechanics* (1995), Volume 285, pp. 69–94.
[22] Haller, G., "An objective definition of a vortex", *Journal of Fluid Mechanics* (2005), Volume 525, pp. 1-26.
[23] Kline, S. J., McClintock, F. A., "Describing Uncertainties in Single-Sample Experiments", *Mechanical Engineering Journal* (January 1953), 3-8, 36310.
[24] Moffat, R. J., "Describing the Uncertainties in Experimental Results", *Experimental and Thermal Fluid Sciences* (1988), Vol. 1, No. 1, pp. 3–17.

[25] Lazar, E., DeBlauw, B., Glumac, N., Dutton, C. and Elliott, G., "A practical approach to PIV uncertainty analysis", 27th AIAA Aerodynamic Measurement Technology and Ground Testing Conference, 28 June- 1 July 2010, Chicago, IL, AIIA Paper 2010-4355.

[26] Sciacchitano, A., "Uncertainty quantification in particle image velocimetry", *Measurement Science and Technology* (2019), 30 092001.

[27] S. J., Wagner, J. L., Pruett, B. O. M., Henfling, J. F., Spillers, R. W., Smith, B. L., "Self-Calibration Performance in Stereoscopic PIV Acquired in a Transonic Wind Tunnel", 30th AIAA Aerodynamic Measurement Technology and Ground Testing Conference, 16-20 June 2014, AIAA Paper 2014-2660.

[28] Raffel, M., C. E. Willert, S. T. Wereley, J. Kompenhans, "Particle Image Velocimetry", Springer-Verlag Berlin Heidelberg, 2007.

[29] Wieneke, B., "PIV uncertainty quantification from correlation statistics", *Measurement Science and Technology* (2015), 26 074002.

[30] Sciacchitano, A., Wieneke., B., "PIV uncertainty propagation", *Measurement Science and Technology* (2016), 27 084006.

[31] Wilson, B. M., Smith B. L., "Uncertainty on PIV mean and fluctuating velocity due to bias and random errors", *Measurement Science and Technology* (2013), 24 035302.

[32] Gupta, R., "Open-Loop and Closed-Loop Trailing Edge Separation Control on a Natural Laminar Flow Airfoil", Master's Thesis, University of Illinois at Urbana–Champaign, Urbana, IL, 2016.

[33] Colletti, C., "Investigating the Frequency Behavior of Fluidic Oscillators and their Applications as Active Flow Control for an SNLF airfoil", Master's Thesis, University of Illinois at Urbana–Champaign, Urbana, IL, 2019.

[34] Ansell, P.J., "Unsteady Modes in the flowfield about an airfoil with a leading-edge horn-ice shape (Doctoral Dissertation)," University of Illinois at Urbana-Champaign, Urbana, IL, 2014.